Eur. Phys. J. D **6**, 29–47 (1999)

THE EUROPEAN PHYSICAL JOURNAL D

EDP Sciences

Semiclassical Monte Carlo approaches for realistic atoms in optical lattices

K. I. Petsas[a], G. Grynberg, and J.-Y. Courtois[b]

Laboratoire Kastler-Brossel, Département de Physique de l'Ecole Normale Supérieure, 24 rue Lhomond, 75231 Paris cedex 05, France

Received: 6 May 1998 / Received in final formed: 21 October 1998

Abstract. We present two different numerical approaches, based on semiclassical Monte Carlo simulations, for the study of optical lattices associated with $J_g \to J_e$ atomic transitions, for angular momenta J_g and J_e larger than $\frac{1}{2}$. Our models rely on an adiabatic-type approximation and give a correct description of the steady-state temperature and localization properties of the lattice, in a large range of parameters. These models combine the possibility of getting intuitive images of complex fundamental physical processes in optical lattices, together with particularly reasonable computing times.

PACS. 32.80.Lg Mechanical effects of light on atoms, molecules and ions – 32.80.Pj Optical cooling of atoms; trapping – 03.65.Sq Semiclassical theories and applications

1 Introduction

The last two decades have been characterized by a considerably growing interest in the field of laser cooling of atoms [1] and in particular in the field of optical lattices [2]. Optical lattices consist of micron-sized ordered atomic samples, originating from the trapping of cold atoms inside potential wells resulting from the interference between several laser beams. In such periodic optical structures, the atoms, bound by the light, principally undergo an oscillatory motion near the bottom of the potential wells [3–5]. The most important experimental studies of optical lattices realized so far dealt with the temperature and localization properties in *bright* [6–10] as well as in *grey* [11–13] one- (1D), two- (2D), or three-dimensional (3D) lattices. Current studies aim also at the characterization of the magnetic [13–16] or of the transport properties of optical lattices [17,18].

The increasing interest for the physics of optical lattices has led to the elaboration of different theoretical models, which permit to explain and predict a great number of experimental observations, in a more or less quantitative manner. The first theoretical considerations in the physics of laser cooled atoms were semiclassical. In such a description, the atoms experience a random force, the average of which is a friction force, and the fluctuations of which lead to atomic momentum diffusion. The approach that is generally used in this case consists in deriving a Fokker-Planck equation [19] from the optical Bloch equations and requires in particular an adiabatic elimination of the rapidly varying internal atomic variables. This "traditional" semiclassical approach was first used in the context of Doppler laser cooling [20–22], and later in the framework of sub-Doppler optical molasses [23–28]. However, it was realized that a more complete theoretical model was necessary in order to give a correct description of the atomic temperature in the low intensity and large detuning range.

An exact resolution method consists in numerically integrating the quantum equations, by propagating in time the density matrix in momentum space, until the system reaches a steady state [29,30]. An alternative procedure for characterizing the physical properties of the atomic system in steady state consists in using the well-known band model [31]. This quantum model was first introduced for the $J_g = \frac{1}{2} \to J_e = \frac{3}{2}$ atomic transition [31,32], then generalized in the case of more complex atomic transitions and used in particular for pump-probe spectroscopy calculations [33]. A third quantum model for the resolution of the optical Bloch equations consists in replacing the atomic density matrix by a set of stochastic wave functions and using quantum Monte Carlo simulation techniques. This method was first introduced by J. Dalibard *et al.* in the general framework of dissipative problems in quantum optics [34], and similar formulations followed for the treatment of particular situations [35]. Such an approach has been consequently used in the framework of 1D [36] and 3D [37] optical lattices leading to temperature

[a] *Present address:* Università degli Studi di Milano, Dipartimento di Fisica, Via Celoria 16, Milano, 20133 Italy. e-mail: `Kostas.Petsas@mi.infn.it`

[b] *Present address:* Thomson-CSF Optronique, Direction Scientifique, rue Guynemer, BP 55, 78283 Guyancourt cedex, France.

evaluations in good agreement with the experimental measurements performed in optical molasses [38] and in optical lattices [39].

Even if the three above-mentioned quantum approaches lead to results which are in good quantitative agreement with the experiments, they all generally involve particularly lengthy numerical calculations. Furthermore, these quantum models occasionally suffer from the difficulty to give simple pictures for the physical mechanisms which are involved in optical lattices, particularly concerning atomic transport phenomena [40].

It is the aim of this paper to present *approximate* semiclassical-like approaches based on Monte Carlo numerical simulations for the study of the atom dynamics in optical lattices. We are interested, in particular, in atomic transitions, between a ground state (g) of angular momentum J_g and an excited state (e) of angular momentum $J_e = J_g+1$, involving large values of J_g, in order to be able to study commonly encountered experimental situations. The models presented in this paper make use of an *adiabatic approximation*, inspired from the Born-Oppenheimer approximation of molecular physics: for a given position of the atom, we first find the energy levels of the system and then simulate the atomic motion in the adiabatic potential associated with these energy levels. The first approach that we present is based on a generalization of the semiclassical method introduced by Castin *et al.* in reference [41] for $J_g = \frac{1}{2}$. In this approach, the atomic motion is simulated in the $(2J_g + 1)$-manifold of optical potential curves. The second approach relies on an *effective bi-potential* method, in which the atomic motion is calculated using two effective potential curves. We compare the results of the two models, for different atomic transitions, and show that they both lead to temperature evaluations in good agreement with the quantum band model for a large range of experimental parameters. Furthermore, we show that such approximate semiclassical approaches permit to obtain new physical insight for complex processes, such as the local cooling mechanism or the paramagnetism of optical lattices. In particular, it is possible within the semiclassical point of view to isolate the effects of the different possible physical factors which act on the atomic motion (optical pumping, radiation pressure, momentum diffusion, anharmonicity of the optical potential) in order to have a better insight in a given physical phenomenon.

The paper is organized as follows. In Section 2, we briefly review the procedure of the adiabatic elimination of the excited state from the generalized optical Bloch equations, which leads to the master equation for the restriction of the density matrix in the ground state. The general lines of the semiclassical formalism used in the paper are presented in Section 3. We then illustrate the semiclassical approach for the 1D lin⊥lin configuration, in the case of the $J_g = \frac{1}{2} \to J_e = \frac{3}{2}$ atomic transition (Sect. 4), and generalize it for larger values of the ground state angular momentum J_g (Sect. 5). In Section 6, we present the effective bi-potential method for $J_g \to J_e = J_g + 1$ transitions, and in Section 7 the results of both models, relative to the atomic temperature, are compared to the quantum band model. A few other illustrations of the semiclassical models are also presented.

2 Master equation for the atomic density matrix

In this section we present some basic notations and then briefly recall the derivation of the master equation for the density matrix of a multilevel atom, starting from the generalized optical Bloch equations. The discussion is restricted to the case of the one-dimensional lin⊥lin laser configuration.

2.1 General

Let us consider the case of a single multilevel atom interacting with a coherent laser field

$$\boldsymbol{\mathcal{E}}_{\mathrm{L}}(\mathbf{r},t) = \frac{1}{2}\mathcal{E}_0\,\boldsymbol{\xi}(\mathbf{r})\,e^{-i\omega_{\mathrm{L}}t} + \text{c.c.}, \tag{1}$$

where $\boldsymbol{\xi}(\mathbf{r})$ is a generally non-normalized dimensionless vector characterizing the spatial profile of the laser polarization and $\mathcal{E}_0$ is an order of magnitude of the electric field amplitude. The density matrix ρ, characterizing the evolution of the atomic system can be written as

$$\rho = \begin{pmatrix} \rho_{\mathrm{gg}} & \rho_{\mathrm{eg}} \\ \rho_{\mathrm{ge}} & \rho_{\mathrm{ee}} \end{pmatrix}, \tag{2}$$

where ρ_{gg} and ρ_{ee} are square arrays containing the populations and the Zeeman coherences, in the ground and in the excited state, respectively, and where $\rho_{\mathrm{eg}} = \rho_{\mathrm{ge}}^{\dagger}$ is a rectangular array, characterizing the optical coherences.

The typical experimental range of variation of the laser intensity and detuning is given by the following two restrictive conditions:

$$s_{\mathrm{L}} \ll 1, \tag{3a}$$

$$|\Delta| \gg \Gamma, \tag{3b}$$

where $s_{\mathrm{L}} = (D\mathcal{E}_0)^2/2(\hbar\Delta)^2$ is the laser saturation parameter expressed in the large detuning limit (*i.e.* when the condition (3b) is fulfilled), D is the dipole moment of the atomic transition, $\Delta = \omega_{\mathrm{L}} - \omega_0$ is the laser detuning from resonance and Γ is the natural width of the excited state. The weak values of the laser intensity ensure the existence of longer characteristic internal times in the evolution of ρ_{gg} compared to the ones for ρ_{ee}. These characteristic times are on the order of the optical pumping time between ground state Zeeman sublevels ($\tau_{\mathrm{p}} \sim 1/\Gamma s_{\mathrm{L}}$), which is much longer than the damping time $1/\Gamma$. As a result, it is possible to adiabatically eliminate the excited state and the optical coherences, and end up with a single master equation relative to the restriction of the atomic density matrix in the ground state ρ_{gg} (in what follows,

we shall use the simpler notation σ for $\rho_{\rm gg}$). This equation reads

$$\frac{\mathrm{d}\sigma}{\mathrm{d}t} = \frac{1}{i\hbar}\left[H_{\rm eff}, \sigma\right] + \left(\frac{\mathrm{d}\sigma}{\mathrm{d}t}\right)_{\rm relax}. \tag{4}$$

The above master equation, can be split into two parts [42]. First, a reactive part, containing the time evolution of σ under the influence of an effective Hamiltonian:

$$H_{\rm eff} = \frac{\mathbf{p}^2}{2M} + \hbar\Delta'\widehat{A}\left(\mathbf{r}\right), \tag{5}$$

where $\mathbf{p}$ is the momentum operator, M the atomic mass and $\mathbf{r}$ the location of the atomic center of mass. This Hamiltonian accounts for the atom kinetic energy (first term of Eq. (5)) and for the light-shifts of the ground state Zeeman sublevels due to the laser field (second term of Eq. (5)). The Hermitian operator

$$\widehat{A}\left(\mathbf{r}\right) = \left[\widehat{\mathbf{d}}^{-}\cdot\boldsymbol{\xi}^{*}\left(z\right)\right]\left[\widehat{\mathbf{d}}^{+}\cdot\boldsymbol{\xi}\left(z\right)\right], \tag{6}$$

introduced above is the so-called light-shift operator [43] ($\widehat{\mathbf{d}}^{+}$ and $\widehat{\mathbf{d}}^{-}$ are the raising and lowering parts of the reduced dipole operator $\widehat{\mathbf{d}} = \mathbf{d}/D$, respectively). A typical order of magnitude for the light-shifts is given by $\hbar\Delta' = \hbar\Delta s_{\rm L}/2$ which is the light-shift undergone by a two-level atom in the presence of a laser field of amplitude $\mathcal{E}_0$. Furthermore, a dissipative part describes the damping of the density matrix under the influence of the different processes of photon absorption and emission:

$$\left(\frac{\mathrm{d}\sigma}{\mathrm{d}t}\right)_{\rm relax} = -\frac{\Gamma'}{2}\left\{\widehat{A}\left(\mathbf{r}\right), \sigma\right\} + \frac{3\Gamma}{8\pi}\int \mathrm{d}^2\Omega_{\boldsymbol{\kappa}} \times \sum_{\boldsymbol{\epsilon}\perp\boldsymbol{\kappa}} \widehat{B}^{\dagger}_{\boldsymbol{\epsilon}}\left(\mathbf{r}\right) e^{-i\boldsymbol{\kappa}\cdot\mathbf{r}}\sigma e^{i\boldsymbol{\kappa}\cdot\mathbf{r}}\widehat{B}_{\boldsymbol{\epsilon}}\left(\mathbf{r}\right), \tag{7}$$

where $\Gamma' = \Gamma s_{\rm L}/2$ is the total photon scattering rate, and where we have introduced the dimensionless non-Hermitian operators $\widehat{B}_{\boldsymbol{\epsilon}}\left(\mathbf{r}\right)$ defined by

$$\widehat{B}_{\boldsymbol{\epsilon}}\left(\mathbf{r}\right) = \left[\widehat{\mathbf{d}}^{-}\cdot\boldsymbol{\xi}^{*}\left(\mathbf{r}\right)\right]\left[\widehat{\mathbf{d}}^{+}\cdot\boldsymbol{\epsilon}\right]. \tag{8}$$

One can notice that in the second term of equation (7), the integration is performed over the solid angle $\Omega_{\boldsymbol{\kappa}}$ in which the fluorescence photon of wave vector $\boldsymbol{\kappa}$ is emitted.

2.2 Case of the lin⊥lin configuration

In the following we shall focus on the case of bright optical lattices (*i.e.* corresponding to $J_{\rm e} = J_{\rm g}+1$), but similar considerations can be developed in the case of grey optical lattices (*i.e.* corresponding to $J_{\rm e} = J_{\rm g}$, or $J_{\rm e} = J_{\rm g}-1$). The laser field configuration considered in this paper is the well-known 1D lin⊥lin configuration [23], which consists of two beams counterpropagating along the z-axis, which have orthogonal linear polarizations (see Fig. 1). The frequency of the incident beams is tuned on the red side of the atomic resonance, so $\Delta = \omega_{\rm L} - \omega_0 < 0$. If we choose the common amplitude of the incident beams to be $E_1 = \mathcal{E}_0/\sqrt{2}$, the total laser field for this configuration is given by equation (1), with a local polarization vector:

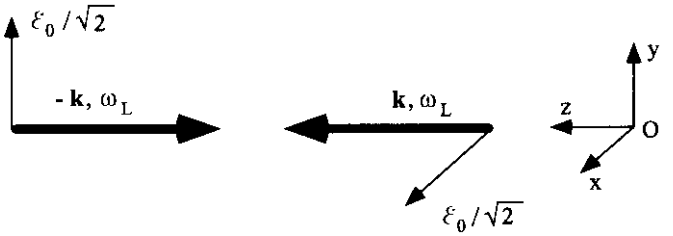

Fig. 1. The lin⊥lin laser field configuration: two laser beams having the same frequency and intensity, but crossed linear polarizations counterpropagate along the Oz axis.

$$\boldsymbol{\xi}\left(z\right) = \cos\left(kz\right)\boldsymbol{\varepsilon}_{-} - i\sin\left(kz\right)\boldsymbol{\varepsilon}_{+}, \tag{9}$$

where $\boldsymbol{\varepsilon}_{\pm}$ are the circular basis unit vectors:

$$\boldsymbol{\varepsilon}_{\pm} = \frac{\mp\mathbf{e}_x - i\mathbf{e}_y}{\sqrt{2}}. \tag{10}$$

We now give the restriction of the master equation in 1D. By integrating equation (7) over the two transverse directions x and y, one gets [31]:

$$\left(\frac{\mathrm{d}\sigma}{\mathrm{d}t}\right)_{\rm relax} = -\frac{\Gamma'}{2}\left\{\widehat{A}\left(z\right), \sigma\right\} + \Gamma'\int_{-\hbar k}^{\hbar k}\mathrm{d}p \times \sum_{q=0,\pm1} N_q\left(p\right)\widehat{B}^{\dagger}_q\left(z\right)e^{-ipz/\hbar}\sigma e^{ipz/\hbar}\widehat{B}_q\left(z\right), \tag{11}$$

where the operators $\widehat{B}_q\left(z\right)$ are expressed in the standard basis of circular polarisation:

$$\widehat{B}_q\left(z\right) = \left[\widehat{\mathbf{d}}^{-}\cdot\boldsymbol{\xi}^{*}\left(z\right)\right]\widehat{d}^{+}_q,\ q = 0, \pm1, \tag{12}$$

and where the angular diagram for spontaneous emission [44] is given by

$$N_{\pm1}\left(p\right) = \frac{3}{8\hbar k}\left(1 + \frac{p^2}{\hbar^2k^2}\right), \tag{13a}$$

$$N_0\left(p\right) = \frac{3}{4\hbar k}\left(1 - \frac{p^2}{\hbar^2k^2}\right). \tag{13b}$$

Note that, following the Wigner-Eckart theorem and the definition of $\widehat{d}$, the matrix elements of the operators $\widehat{d}^{+}_q = \widehat{\mathbf{d}}^{+}\cdot\boldsymbol{\varepsilon}_q$ (where $q = 0, \pm1$) are simply given by

$$\left\langle J_{\rm e}\, M_{\rm e}\right|\widehat{d}^{+}_q\left|J_{\rm g}\, M_{\rm g}\right\rangle = \left\langle J_{\rm g}\, 1\, M_{\rm g}\, q\right|\left.J_{\rm e}\, M_{\rm e}\right\rangle, \tag{14}$$

where $\left\langle J_{\rm g}\, 1\, M_{\rm g}\, q\right|\left.J_{\rm e}\, M_{\rm e}\right\rangle$ is the Clebsch-Gordan coefficient connecting the sublevels $\left|J_{\rm g},\, M_{\rm g}\right\rangle$ and $\left|J_{\rm e},\, M_{\rm e} = M_{\rm g} + q\right\rangle$.

The optical pumping equation (4) which characterizes the internal and external dynamics of an atom interacting with the laser field (1) is the starting point for any

calculation relative to the atomic system. We shall now introduce the semiclassical approaches used for numerically integrating this equation and getting information on the stationary properties of the atomic ensemble. The two cases of $J_g = \frac{1}{2}$ and $J_g > \frac{1}{2}$ will be distinguished and discussed separately in the following sections.

3 The general formalism of the semiclassical approach

Let us first discuss the basic steps of the procedure used to investigate the semiclassical limit of the master equation. In this limit, because the atomic momentum distribution has a smooth variation at the scale of the photon momentum, it is possible to derive a Fokker-Planck-type equation for the time evolution of the semiclassical phase-space distribution. The Wigner representation [45] is particularly well suited to this treatment [46]. In this representation, a $[(2J_g+1)+(2J_e+1)]^2$-dimensional array $W(\mathbf{r},\mathbf{p},t)$ is associated with the density operator $\rho(t)$. For the 1D situations presented in this paper we will consider the restriction of the Wigner matrix in the ground state and in 1D. This matrix, $w(z,p,t)$, representing a quasi-probability distribution in phase space, is defined by

$$w(z,p,t) = \frac{1}{2\pi\hbar}\int \mathrm{d}u \ \left\langle z+\tfrac{1}{2}u\right| \sigma(t) \left|z-\tfrac{1}{2}u\right\rangle \exp\left(-\tfrac{ip\cdot u}{\hbar}\right). \tag{15}$$

By considering the Wigner transform of equation (4) and by using equation (11), we obtain an equation for the time evolution of the quasi-probability density $w(z,p,t)$. In all this paper we will limit ourselves to situations where the variations of the atomic momentum distribution during such elementary processes are negligible when compared to the width of this distribution:

$$\Delta p \gg \hbar k. \tag{16}$$

This also means that $k\Delta\xi \ll 1$, $\Delta\xi$ being the spatial coherence length of the atomic wavepacket.

The restrictive condition (16) allows for expanding all terms in the equation of evolution of w, up to second order in $\hbar k/\overline{p}$ ($\overline{p}$ being the r.m.s. atomic momentum); for example:

$$w(z,p\pm\hbar k,t) \simeq w(z,p,t) \pm \hbar k\frac{\partial}{\partial p}w(z,p,t) + \frac{(\hbar k)^2}{2}\frac{\partial^2}{\partial p^2}w(z,p,t). \tag{17}$$

We now examine more precisely the nature of the resulting equation of motion, as well as its numerical solution, in the case where $J_g = \frac{1}{2}$ [41,47], and then for $J_g \geq 1$.

4 Case of the $J_g = \frac{1}{2} \rightarrow J_e = \frac{3}{2}$ atomic transition

4.1 Nature of the equations

The simplest atomic transition leading to a bright optical lattice in the case of the lin⊥lin configuration is the $J_g = \frac{1}{2} \rightarrow J_e = \frac{3}{2}$ transition. The treatment of this transition within the semiclassical framework does not present any major difficulty, since there are only two magnetic levels in the ground state and there is no Zeeman coherence between these two levels (given the fact that the light field does not induce couplings between the two states $\left|g, m=+\frac{1}{2}\right\rangle$ and $\left|g, m=-\frac{1}{2}\right\rangle$, the restriction of the atomic density matrix in the ground state is indeed diagonal). The matrix $w(z,p,t)$ is also diagonal in the basis $\left|g, m=\pm\frac{1}{2}\right\rangle$. As a result, in the semiclassical limit one can identify the quasi-probability distributions $w_{m=\pm}(z,p,t)$ to semiclassical "populations" $\Pi_\pm(z,p,t)$. In this case, the phenomenological equations characterizing the time evolution of the quantities $\Pi_\pm$ take the following suggestive form:

$$\left[\frac{\partial}{\partial t} + \frac{p}{M}\frac{\partial}{\partial z} - \frac{\mathrm{d}U_\pm(z)}{\mathrm{d}z}\frac{\partial}{\partial p}\right]\Pi_\pm(z,p,t) = -\left[\gamma_{\pm\mp}(z)\Pi_\pm(z,p,t) - \gamma_{\mp\pm}(z)\Pi_\mp(z,p,t)\right] + \frac{\partial^2}{\partial p^2}\left[D_{\pm\pm}(z)\Pi_\pm(z,p,t) + D_{\mp\pm}(z)\Pi_\mp(z,p,t)\right], \tag{18}$$

where $U_\pm(z) = \frac{U_0}{2}\left[-2\pm\cos(2kz)\right]$ is the optical bi-potential ($U_0 = -2\hbar\Delta'/3$ being the optical potential well depth [31]) and where

$$\gamma_{\pm\mp}(z) = \frac{\Gamma'}{9}\left[1\pm\cos(2kz)\right], \tag{19a}$$

$$D_{\pm\pm}(z) = \frac{7\hbar^2k^2\Gamma'}{90}\left[5\pm\cos(2kz)\right], \tag{19b}$$

$$D_{\pm\mp}(z) = \frac{\hbar^2k^2\Gamma'}{90}\left[6\mp\cos(2kz)\right]. \tag{19c}$$

The interpretation of equation (18) is quite intuitive [19]. It corresponds to the Brownian motion of a (classical) particle inside the bi-potential $U_\pm(z)$:

– To zeroth order in $\hbar k/\overline{p}$, one obtains the *classical* equations characterizing the effect of optical pumping between the ground state Zeeman sublevels, for a free particle of constant velocity (note that $\frac{\partial}{\partial t} + \frac{p}{M}\frac{\partial}{\partial z}$ is simply the convective derivative $\frac{\mathrm{d}}{\mathrm{d}t}$ for a free particle). The rates $\gamma_{+-}(z)$ and $\gamma_{-+}(z)$ determine the probability per unit time for a change of the Zeeman sublevel (spin flip) for each point in space. These quantities are proportional to the optical pumping rate of the $\frac{1}{2} \rightarrow \frac{3}{2}$ transition, $\gamma_0 = \frac{2}{9}\Gamma'$. Moreover, following equation (19a), γ_{+-} (resp. γ_{-+}) is zero in sites where the light polarization is purely σ^+ (resp. σ^-), which is quite intuitive.

– To first order in $\hbar k/\overline{p}$, equation (18) corresponds to the atomic motion in the presence of the mean radiative force $\mathbf{F}_{\pm}(z) = -\frac{\mathrm{d}U_{\pm}(z)}{\mathrm{d}z}\,\mathbf{e}_z$, which is the first derivative of the optical potential.
– Second order in $\hbar k/\overline{p}$ corresponds to the process of momentum diffusion, characterizing the effect of heating along the Oz axis during a fluorescence cycle. The coefficients $D_{mm}(z)$ represent the diffusion due to random momentum jumps resulting from spontaneous emission of circularly polarized photons (during such processes the atom does not undergo a change of internal level $|m\rangle$). By contrast, the coefficients $D_{mm'}(z)$ with $m \neq m'$ are related to fluorescence cycles where the atom, after having absorbed a circularly polarized photon, undergoes a change of magnetic sublevel by emitting a photon of linear π-polarization.

4.2 Integration of the equations of motion

The study of the stochastic process represented by equation (18) is being performed using Monte Carlo simulation techniques. In order to obtain the algorithm of the simulation, it is convenient to expand the semiclassical equations of motion in successive powers of the dimensionless parameter $\epsilon = \Gamma' \cdot \mathrm{d}t \ll 1$, $\mathrm{d}t$ being the elementary time step of integration. Suppose for instance that the atom initially populates the Zeeman level $|+\rangle$ at time t. The equation of motion (18) is equivalent to the stochastic process:

$$\mathrm{d}z(t) = \frac{p(t)}{M}\mathrm{d}t, \tag{20a}$$

$$\mathrm{d}p(t) = -\frac{\mathrm{d}U_+}{\mathrm{d}z}\mathrm{d}t + \theta(r - \gamma_{+-}\mathrm{d}t)\, f_+ \mathrm{d}t + [1 - \theta(r - \gamma_{+-}\mathrm{d}t)]\,\delta p_-\,, \tag{20b}$$

where $\theta(x) = 1$ for $x > 0$ and $\theta(x) = 0$ else, and where the random variables $f_\pm$ and $\delta p_\pm$ have been introduced in order to simulate the random momentum kicks undergone by the atom due to photon exchange with the field. These variables are related to the different momentum diffusion coefficients of equation (18) by

$$\langle f_\pm(z)\rangle = 0 \quad \text{and} \quad \langle f_\pm^2(z)\rangle = \frac{2D_{\pm\pm}(z)}{\mathrm{d}t}, \tag{21a}$$

$$\langle \delta p_\pm(z)\rangle = 0 \quad \text{and} \quad \langle \delta p_\pm^2(z)\rangle = \frac{2D_{\mp\pm}(z)}{\gamma_{\pm\mp}(z)}. \tag{21b}$$

Let us underline that $\gamma_{+-}\mathrm{d}t$ is the probability that the atom has left the level $|+\rangle$ after a time step (*i.e.* at $t + \mathrm{d}t$) and that the variable $\varpi_+ = \theta(r - \gamma_{+-}\mathrm{d}t)$ goes to zero with this same probability (*i.e.* $\varpi_+ = 0$ if the random number generator leads to a real number r such that $r < \gamma_{+-}\mathrm{d}t$). For the numerical integration of equations (20a-b), we use a second order Runge-Kutta algorithm. This choice has been made in order to obtain sufficiently precise numerical results, in an optimum computing time.

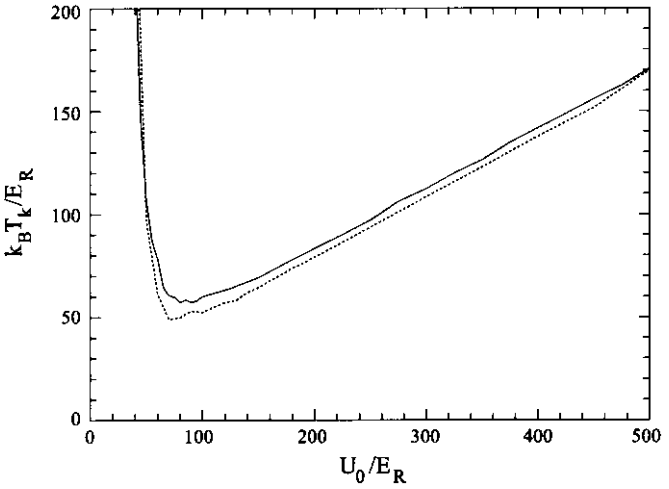

Fig. 2. Variation of the kinetic temperature as a function of the potential well depth U_0 (in recoil units) in the case of the $J_\mathrm{g} = \frac{1}{2} \rightarrow J_\mathrm{e} = \frac{3}{2}$ atomic transition. The full line represents the result of the semiclassical Monte Carlo simulation, whereas the dotted one represents the quantum result of the band model. The numerical simulation involves a sample of $N_0 = 5000$ atoms, an averaging time of $1000/\Gamma'$ after an evolution time of $2000/\Gamma'$ in order to reach steady state, and has been performed for a laser detuning $\Delta = -10\Gamma$. The quantum calculation is performed within the framework of the secular approximation and takes into account the first 80 band states.

4.3 Temperature calculations

The numerical integration of the equation of motion using the semiclassical Monte Carlo simulation allows one to obtain the steady-state values of the probability distributions $\Pi_m(z, p, t)$. These distributions give access to all relevant physical quantities characterizing the lattice. In order to illustrate the semiclassical approach in the case of $J_\mathrm{g} = \frac{1}{2}$, we present in Figure 2 the calculated variation of the atomic kinetic temperature with the (dimensionless) potential well depth U_0/E_R. The kinetic temperature T_k is defined in 1D as follows:

$$\frac{1}{2}k_\mathrm{B}T_\mathrm{k} = \frac{\overline{p}^2}{2M}. \tag{22}$$

We have also represented in the same figure (dotted line) the numerical result of the quantum band model, introduced in reference [31]. By comparing the two curves, one observes an excellent quantitative agreement between the semiclassical and the quantum approaches, for the values of the optimum temperature, as well as for the slopes of the linear parts of the curves.

By performing similar numerical calculations on other relevant observables of the atomic motion, such as the steady-state spatial or momentum distributions, or the spatial diffusion coefficient in the diffusive regime [18], or even the fluorescence spectra of the lattice [47], and by comparing the results to the quantum ones, one could easily convince oneself that the semiclassical approach leads to an excellent quantitative agreement with the quantum calculations. In fact, the case of $J_\mathrm{g} = \frac{1}{2}$ corresponds to

a particular situation where the density matrix, as well as the Wigner function, are both diagonal in the ground state and therefore the semiclassical approach is rigorous (to second order in $\hbar k/\overline{p}$).

5 Case of angular momenta $J_g > \frac{1}{2}$

A great number of numerical calculations relative to bright optical lattices performed so far has been based on the $J_g = \frac{1}{2} \rightarrow J_e = \frac{3}{2}$ model atomic transition that was briefly examined in the previous section. However, as it has been pointed out by Meacher *et al.* [14] and by Mennerat-Robilliard *et al.* [15], several important physical properties such as the paramagnetism of optical lattices cannot be understood within the framework of this simple atomic transition. This section is devoted to the presentation of a first semiclassical treatment suited to more realistic atomic transitions.

By contrast to the $J_g = \frac{1}{2}$ case, the situation is more complex for a general $J_g = J \rightarrow J_e = J + 1$ atomic transition, where $J_g \geq 1$, because of the existence of many magnetic sublevels in the ground state and because of the presence of Zeeman coherences between these levels. The two different methods that we use for overcoming these difficulties rely both on the adiabatic approximation. We first introduce this approximation and qualitatively discuss its range of validity. Then we present the two numerical approaches and compare the obtained results.

5.1 Adiabatic potentials and motional coupling: the adiabatic approximation

In the case of bright optical lattices operating on $J_g = J \rightarrow J_e = J+1$ atomic transitions (with $J \geq 1$) and in the 1D lin⊥lin laser field configuration, the light-shift operator is not diagonal in the $|J_g, m_g\rangle$ basis. However, because of the absence of π-polarized light occurring for this particular configuration, only Zeeman sublevels of the ground state having magnetic quantum numbers of the same parity $(-1)^{(m_g - J_g)}$ are mutually coupled by light. One therefore distinguishes two families $\eta = 1, 2$ of Zeeman sublevels, with respect to the parity of the magnetic number. By diagonalizing the light-shift operator, one obtains the different curves $u_m(z)$ of the so-called "*adiabatic*" potential. Figure 3 illustrates this potential for the cases of the $J_g = 1 \rightarrow J_e = 2$ and of the $J_g = 4 \rightarrow J_e = 5$ transitions. One notices in particular that for a given family (same grey hue on the figure) the potential curves present avoided crossings. These avoided crossings are due to Raman couplings between the different Zeeman sublevels. The $\lambda/4$ spatial periodicity of the avoided crossings is the same as the one of the potential wells, but the locations of the avoided crossings are shifted by $\lambda/8$ with respect to the position of the wells. Moreover, one can note that the lowest potential curve, exhibiting a spatial alternation of σ^+ and σ^- polarized sites with a $\lambda/4$ period, does not cross any other potential curve at any point. As a result, one may think in a first approach that a moving atom can

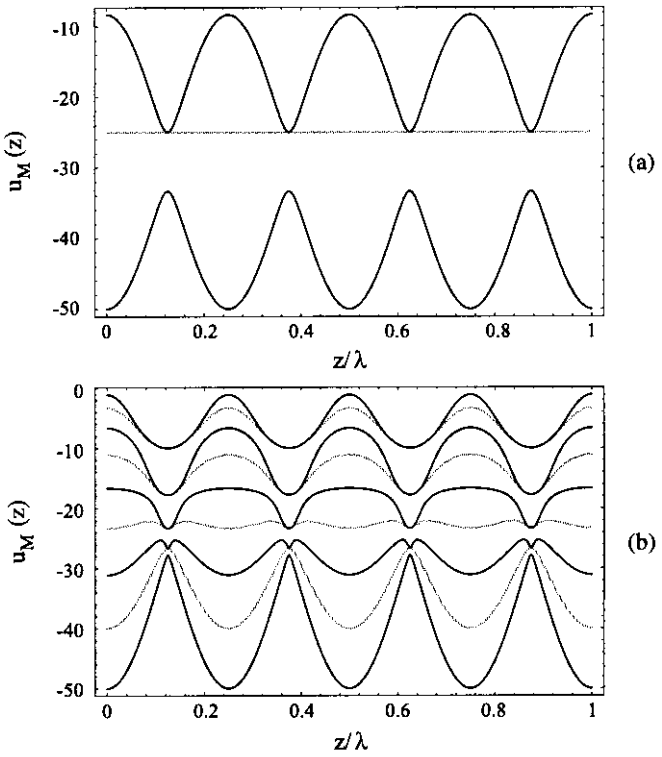

Fig. 3. Adiabatic optical potentials for $J_g = 1 \rightarrow J_e = 2$ (a) and $J_g = 4 \rightarrow J_e = 5$ (b) transitions. The potentials are obtained by diagonalizing the light-shift operator given by equation (5). For both cases, we distinguish by using different grey hues for the two different sets of levels $\eta = 1, 2$. Only magnetic levels that belong to the same set η are coupled *via* the light. The light-shifts are given in recoil energy units, and the z-abscissa is given in optical wavelength (λ) units. The figure has been obtained for $\hbar\Delta' = -50E_R$.

follow adiabatically this potential curve, travelling along a σ^+ and σ^- site succession, while undergoing in some specific locations an optical pumping cycle to another potential curve. In a more precise approach, one would have to take correctly into account the kinetic energy of the atoms. In fact, the atomic motion induces additional couplings between the optical potential curves, which lead to non-adiabatic transitions [48] between the different eigenstates of the light-shift operator.

In all the following, we suppose that each atom adiabatically follows its internal state. This assumption consists in neglecting all motion-induced couplings between the different potential curves. Despite the fact that such an approximation may appear somehow rough in a first view, particularly for the case of fast atoms, it turns out that it leads to a satisfactory description of the atomic motion, at least in the limit of deep potential wells. It is, indeed well-known from the band model [31] that in this regime the atoms are mostly localized in the vicinity of the bottom of the potential wells where the probabilities of non-adiabatic transfers between the different potential curves are very weak. Furthermore, the use of the adiabatic approximation will be justified *a posteriori*,

since we will show that in the regime of very deep potential wells the energy damping mechanism is principally *local* for $J \to J+1$ transitions with $J > 1$ (see Section 7.2). As a consequence, our model should be satisfactory for giving qualitative descriptions of the basic physical mechanisms, that do not explicitly involve atomic jumps between adjacent potential wells. For instance, one should exclude the study of the transport phenomena in optical lattices, since the non-adiabatic transitions between the potential curves may be essential for the atomic transport.[1]

Furthermore, we introduce also a secular-type approximation in our treatment. This approximation consists in assuming that the Wigner matrix $w(z,p,t)$ is diagonal in the basis of the adiabatic states $|\Phi_i\rangle$ (eigenstates associated with the potential curves u_i). This assumption relies on the fact that the optical pumping rates between the different levels are small with respect to the level-energy-splitting and is generally satisfactory in the case of bright lattices operating in the deep potential well regime [50]. Some elements of a more complete treatment are given in Appendix **B**.

5.2 Model taking into account all adiabatic potential curves

A natural first attempt for generalizing the approach of Section 4 for atomic transitions involving high values of the ground state angular momentum J_g consists of considering the whole set of the adiabatic potential curves in the semiclassical equation for the atomic motion. However, by contrast to the case of the $J_g = \frac{1}{2} \to J_e = \frac{3}{2}$ transition, the adiabatic potentials cannot be generally casted in an analytical manner.

The general steps of the method used for deriving an equation of motion for the Wigner quasi-probability density has been exposed in Section 3. First, the master equation (4) is expressed in the Wigner representation. Then, the non-local terms in momentum space involved in the evolution equation of $w(z,p,t)$ are expanded up to the second order in $\hbar k/\overline{p}$ and the integration along the emission direction of the fluorescence photon is performed, taking into account the angular diagram for spontaneous emission (13a-b). The equation of motion obtained in this manner is consequently expressed for each internal adiabatic sublevel $|\Phi_m\rangle$, associated with the potential curve $u_m(z)$.

As mentioned above, we neglect the non-diagonal elements of the Wigner matrix on the basis of the adiabatic states. It is then straightforward to show that the resulting equations of motion can be expressed as a system of linear coupled differential equations on the quasi-probability densities $\Pi_i(z,p,t) = \langle\Phi_i| w(z,p,t) |\Phi_i\rangle$ of the different adiabatic sublevels of the ground state:

$$\left[\frac{\partial}{\partial t} + \frac{p}{M}\frac{\partial}{\partial z} - \frac{\mathrm{d}u_i(z)}{\mathrm{d}z}\frac{\partial}{\partial p}\right]\Pi_i(z,p,t) = -\left[\gamma_i(z)\,\Pi_i(z,p,t) - \sum_{j\neq i}\gamma_{ji}(z)\,\Pi_j(z,p,t)\right] + \frac{\partial^2}{\partial p^2}\left[D_{ii}(z)\,\Pi_i(z,p,t) + \sum_{j\neq i} D_{ji}(z)\,\Pi_j(z,p,t)\right]. \quad (23)$$

These equations have a similar structure to the ones of equation (18), which were derived in the case of the $\frac{1}{2} \to \frac{3}{2}$ transition. However, each adiabatic level is now potentially coupled to all the other levels *via* the optical pumping term (second term of the second member of Eq. (23)), as well as *via* the momentum diffusion term associated with a change of adiabatic level (fourth term of the second member of Eq. (23)). Naturally, there is no simple analytical expression for the different coefficients involved in the above equations of motion, because there is none for the $|\Phi_i\rangle$ and u_i. Some general expressions for these coefficients are given in Appendix **C**. Let us also note that the coefficients D_{ji} lead generally to very small corrections of the values of the kinetic temperature calculated by taking into account only the coefficients D_{ii}. This is because in steady state, momentum diffusion associated with a change of adiabatic sublevel is a relatively rare event, because of the Lamb-Dicke effect [5]. The D_{ji}'s have been consequently neglected in the calculations presented here.

We have now all the necessary elements for the realization of a semiclassical simulation for atomic transitions connecting high angular momentum states. However, before presenting the results of such a simulation, we proceed in the following section to a different formulation of the model, simplifying the form of the equations of motion (23), which are consequently reduced in number and put in the form of equations (18). For this alternative formulation, only two effective potential levels are involved. The results of the two different approaches are then presented in Section 7, and particular illustrations of the atom dynamics in 1D optical lattices are given.

6 The effective bi-potential method

In our second approach we adopt a "mean potential" point of view: we replace the multitude of the internal atomic levels by two *effective* potential curves accounting for the effect of the whole set of the adiabatic potentials on the atomic motion. The choice of this approach is suggested by the fact that, as it has been shown using the quantum band model [31,32], the greatest fraction of the atoms within the lattice populate the lowest band energy levels, which are associated with the lowest adiabatic potential curve. This means, in a semiclassical language, that the atom dynamics is dominated by an evolution within

[1] One can note incidentally that a recent experiment [49] using chromium atoms on a $J_g = 3 \to J_e = 4$ transition has shown that despite the existence of non-adiabatic transitions, the atomic motion can be generally well described in the framework of the adiabatic approximation.

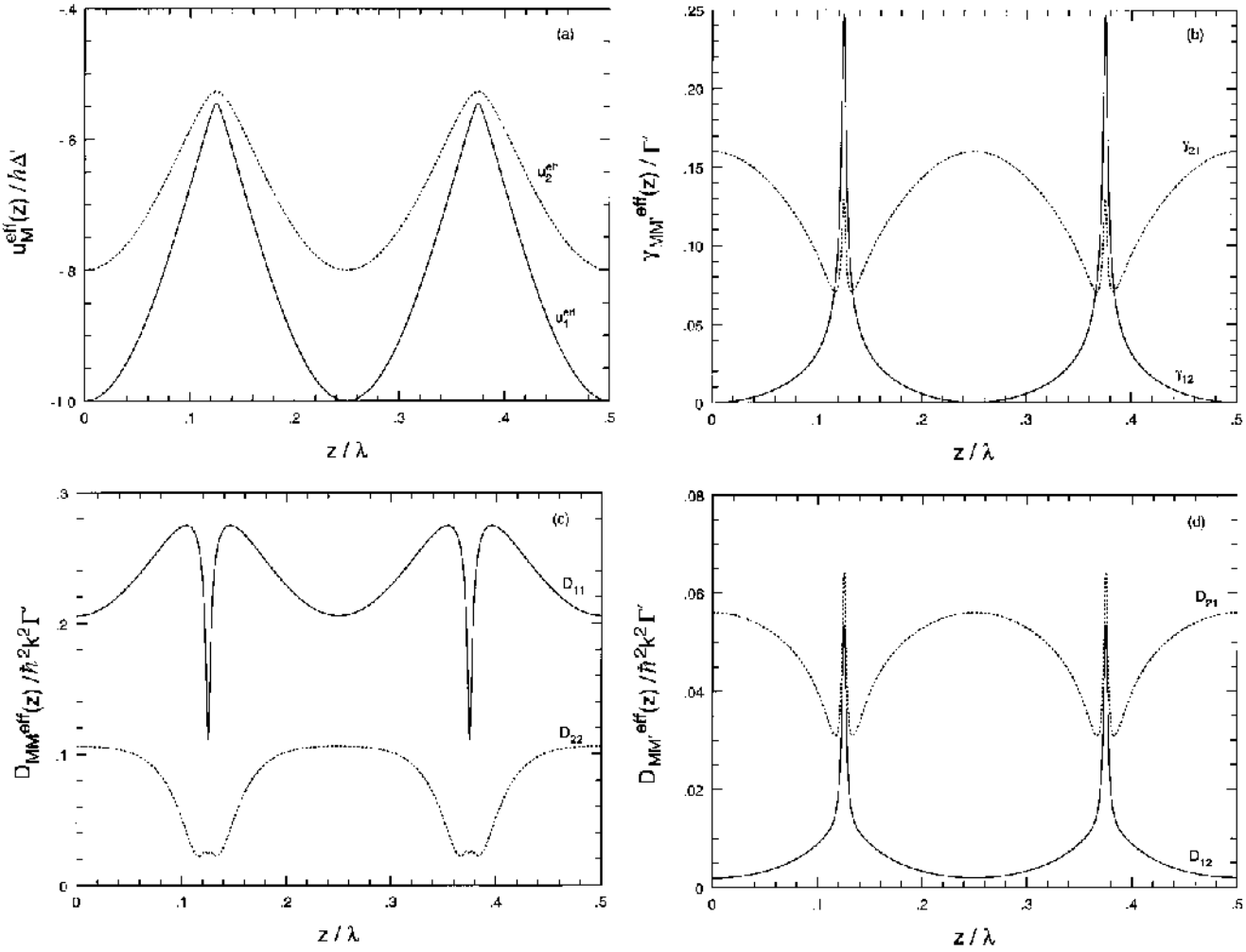

Fig. 4. Effective bipotential and associated coefficients in the case of the $J_g = 4 \rightarrow J_e = 5$ atomic transition. (a) Effective bipotential. The two curves have been obtained by numerically integrating the expressions of the effective radiative forces given by equations (24a-b). (b) Effective optical pumping rates. (c) Momentum diffusion coefficients: diagonal terms. (d) Momentum diffusion coefficients: non-diagonal terms.

the lowest potential curve, the other states being involved episodically during optical pumping jumps of the atom. Therefore, it may appear reasonable to keep the lowest potential curve[2] $u_1(z)$ unchanged, while replacing the other levels by an effective potential curve. In order to optimize the choice of this effective potential curve, one should take into account the fact that the longer an atom occupies a given adiabatic level the more important this level is to the cooling mechanism. We therefore evaluate the effective radiative force (mean classical force associated with the effective potential curve $u_2^{\rm eff}$) by taking the average of the forces associated with each of the adiabatic curves, except u_1, weighted by the *steady-state* occupation rates for an atom at rest $\pi_M^{\rm st}(z)$ of each curve[3]:

$$\mathbf{F}_1^{\rm eff}(z) = \boldsymbol{\nabla} u_1(z), \tag{24a}$$

$$\mathbf{F}_2^{\rm eff}(z) = \frac{\sum_{M\neq 1} \pi_M^{\rm st}(z)\, \boldsymbol{\nabla} u_M(z)}{\sum_{M\neq 1} \pi_M^{\rm st}(z)}. \tag{24b}$$

It becomes possible within this treatment to replace equation (23), by the equation of motion of an atom evolving inside the effective bi-potential $u_{1,2}^{\rm eff}$ associated with the effective forces (24a) and (24b). This equation of motion has the same structure as equation (18), obtained in the case of the $\frac{1}{2} \rightarrow \frac{3}{2}$ atomic transition. Therefore, our procedure considerably simplifies the treatment, since we are now led to the resolution of two coupled linear differential equations (one for each effective potential curve),

[2] In the case where J_g is an integer, the lowest potential curve $u_1(z)$ is well isolated. We implicitely consider this situation. However, an effective bi-potential can also be found when J_g is half-integer.

[3] This averaging method may remind one of the dipole potential for two-level atoms (see, *e.g.*, Ref. [51]).

instead of the $2J_g + 1$ coupled equations of the previous section. The various relevant semiclassical coefficients of the atomic motion (radiative forces, optical pumping rates, momentum diffusion coefficients) are also calculated making use of the averaging method of equation (24b). We have represented the spatial variations of these coefficients in Figure 4, for the $J_g = 4 \to J_e = 5$ atomic transition. As it can be noticed, in Figure 4(a) we have plotted the two curves of the effective bi-potential, $u^{\text{eff}}_{1,2}$, which are the primitives of the forces $\mathbf{F}^{\text{eff}}_1$ and $\mathbf{F}^{\text{eff}}_2$, instead of ploting the forces, since these curves can be directly compared to those of the adiabatic potentials of Figure 3(b). Several interesting features can be seen in the figure:

- First, the effective potential curve u^{eff}_2 reminds closely the adiabatic curve u_2, whereas $u^{\text{eff}}_1 = u_1$ (see, *e.g.*, Eq. (24a)). One expects indeed the other higher-energy potential curves not to be substantially involved in the motion of a slow atom.
- Second, the departure rate from the curve u^{eff}_1 towards the curve u^{eff}_2 due to optical pumping (γ^{eff}_{12}) exhibits very sharp maxima near the edges of the potential curve u_1, while its value remains very small outside these regions. By contrast, the departure rate γ^{eff}_{21} is maximum near the bottom of the deepest potential wells, which simply indicates that the semiclassical probability to find an atom on the lowest potential curve is maximum near these points where the light is circularly polarized.
- One can also notice that the effective diffusion coefficients D^{eff}_{ij} $(i, j = 1, 2)$ associated with a change of potential curve seem to be nearly proportional to the optical pumping rate[4]. However, a more careful look at the figure permits to see that signatures of quantum effects similar to photon diffusion at the nodes of a standing wave persist. For instance, the coefficient D_{12} does not vanish completely in locations where the probability for an atom to switch from the curve u_1 to the curve u_2 is zero (*i.e.* at the bottom of the deepest potential wells where the polarization is purely circular). As has been mentioned above, such momentum diffusion coefficients associated with a change of effective potential curve will be systematically neglected.

Naturally, one may argue that our effective potential definition resulting from equations (24a-b) is not unique. For instance, one could think of evaluating a mean potential level for each of the two families of internal states $\eta = 1, 2$, defined with respect to the parity of the magnetic sublevel. Nevertheless, when taking into account the quantum calculations relative to stationary energy level populations, one may easily be convinced that most of the atoms populate energy levels associated with the lowest adiabatic potential curve. As a result, it is more likely to give a realistic description of the atomic motion when taking correctly into account the contribution of this level.

[4] We remind that for a classical stochastic process one has [19]: $D_{ij} \sim q^2\gamma_{ij}$, where $q \in \mathbb{R}$.

7 Results, comparison and illustrations

7.1 Results and comparison

We now turn to the results of the numerical simulations and to the comparison between the two models introduced in the previous sections (adiabatic potentials or effective bi-potential methods). We have performed numerical calculations relative to the variation of the kinetic temperature with the potential well depth, to the spatial distribution of the atoms inside the lattice and to the atomic momentum distribution profile in steady state. For illustration purposes, we shall focus our discussion on the case of the cesium $J_g = 4 \to J_e = 5$ transition. However, the results relative to temperature calculations performed for other atomic transitions are also presented.

The numerical resolution of the equation of motion (using the exact adiabatic potentials or the effective bi-potential) is carried out by means of a semiclassical Monte Carlo simulation. The basic idea of the algorithm has already been developed in Section 4 for the $\frac{1}{2} \to \frac{3}{2}$ transition. There is, however, an important difference in the present case, which is that the relevant semiclassical coefficients involved in the equations of motion cannot be calculated in an analytical manner. In order to overcome this problem, we numerically evaluate the variation of these coefficients as a function of z over a spatial period of the lattice. The spatial step of the grid that we consider is $\lambda/2000$. We thus first generate a discrete "database" containing the spatial variations of the optical pumping rates, the momentum diffusion coefficients and of the components of the radiative force for each internal level. Second, we proceed to the simulation of the atomic trajectories using a second order Runge-Kutta algorithm for integrating the equations of motion. It is therefore necessary to evaluate the various relevant semiclassical coefficients of the atomic motion at each point $z_i(t)$ of a trajectory. For this we use a linear interpolation method between the two closest points of the previously constructed discrete "database".

7.1.1 Kinetic temperature; comparison between the different models

First, we present a systematic study of the variation of the kinetic temperature as a function of the potential well depth, performed for different atomic transitions. Figure 5 shows the results obtained for $J_g = J \to J_e = J+1$ transitions, for ground state angular momenta $J = 1, 2, 3$ and 4. Our numerical calculations correspond to a laser detuning of $\Delta = -10\Gamma$, and have been averaged over 5000 atoms for a time interval corresponding to $1000/\Gamma'$ in the stationary regime. We have plotted on each graph the curves corresponding to the adiabatic potential calculation, those calculated using an effective bi-potential method, as well as the results obtained by using the quantum band model. This allows to perform comparisons, as well as to test the accuracy of our models.

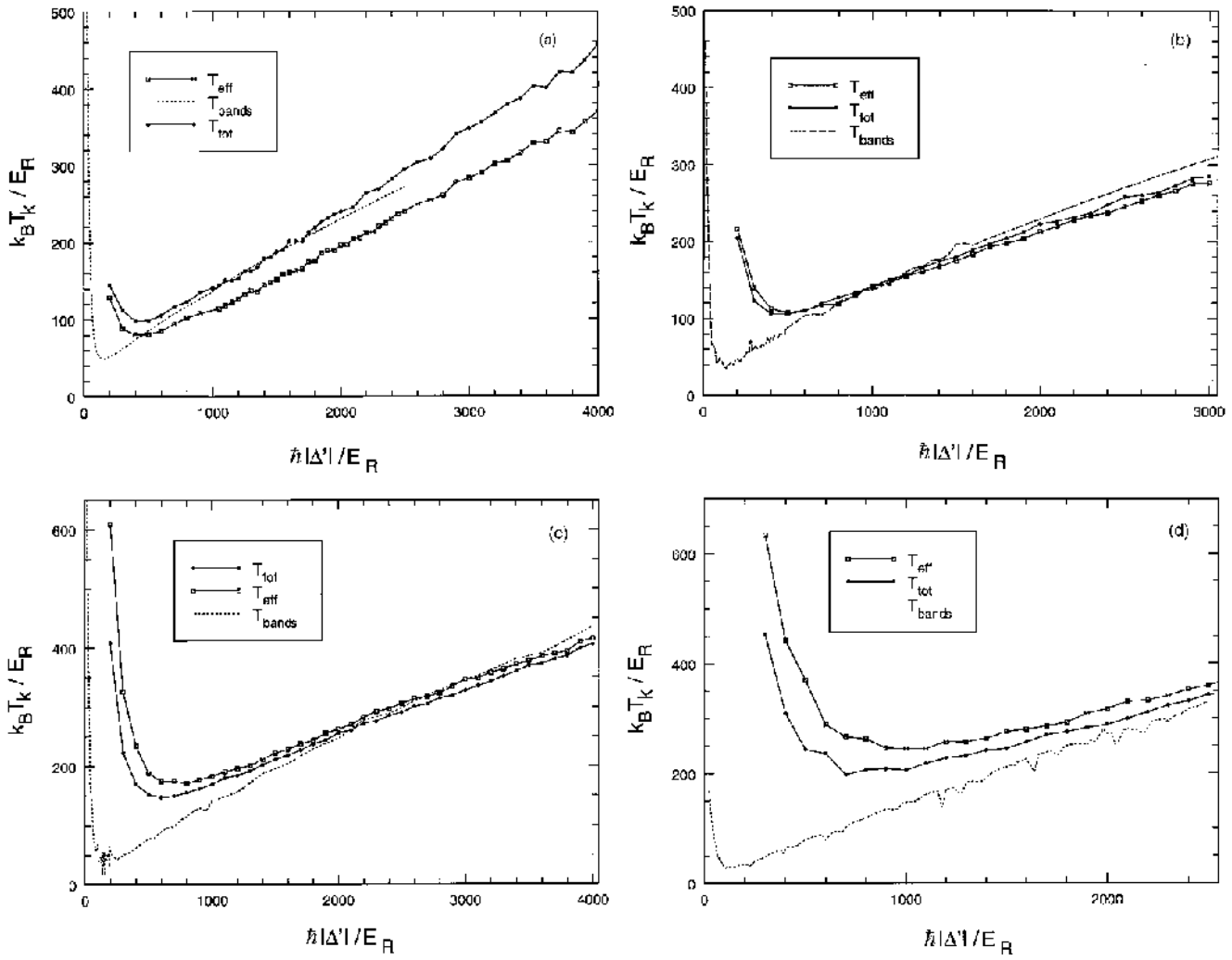

Fig. 5. Kinetic temperature as a function of the optical potential well depths calculated for several atomic transitions; comparison between the different numerical models. (a) $J_g = 1 \rightarrow J_e = 2$ transition, (b) $J_g = 2 \rightarrow J_e = 3$ transition, (c) $J_g = 3 \rightarrow J_e = 4$ transition, (d) $J_g = 4 \rightarrow J_e = 5$ transition. $T_{\rm bands}$ is the curve obtained using the band model in the framework of the secular approximation, $T_{\rm tot}$ corresponds to the semiclassical model taking into account the whole set of the adiabatic potentials, and $T_{\rm eff}$ is the result of the effective bi-potential semiclassical model. The semiclassical calculations have been performed for a laser detuning of $\Delta = -10\Gamma$, with a sample of 5000 atoms. The averaging time is $1000/\Gamma'$, after an evolution of the atomic system (in order to reach the steady state) of $3000/\Gamma'$.

First of all, one notices that apart from the case of the $J_g = 1 \rightarrow J_e = 2$ transition, there is a very good agreement between the effective bi-potential model and the adiabatic potential one. This is of course a favourable argument for the use of the effective bi-potential model. It should be noticed that the $1 \rightarrow 2$ transition is a particular case, which must be considered separately. In fact, the spatial structure of the adiabatic potential shown in Figure 3(a) differs substantially from the ones of the $J \rightarrow J+1$ transitions, involving $J > 1$ (see, *e.g.*, Fig. 3(b)). In particular, the minima of the adiabatic potential curve u_3 (highest potential curve) do not coincide with those of the curve u_1 (lowest potential curve) and the potential curve u_2 is not modulated in space. As a result, one expects in this case the atomic semiclassical trajectories to be more or less similar to those obtained in the case of the $J_g = \frac{1}{2} \rightarrow \frac{3}{2}$ transition and in particular the atom to spend relatively long time intervals on each of the adiabatic levels of the optical potential. This means that the detail of the spatial variation of the whole set of the adiabatic potential curves is essential for the atomic motion. Therefore, the effective bi-potential approach constitutes a rather rough approximation in this case.

Second, we compare the results of the semiclassical simulations to those of the band model [31], in order to have a more precise idea of the validity domain, as well as of the degree of credibility that one should associate with the semiclassical approximation. For each of the atomic transitions that we have considered, the results obtained using the band model have been represented with dashed lines in Figure 5. A very good agreement is found between the quantum and semiclassical models in the deep

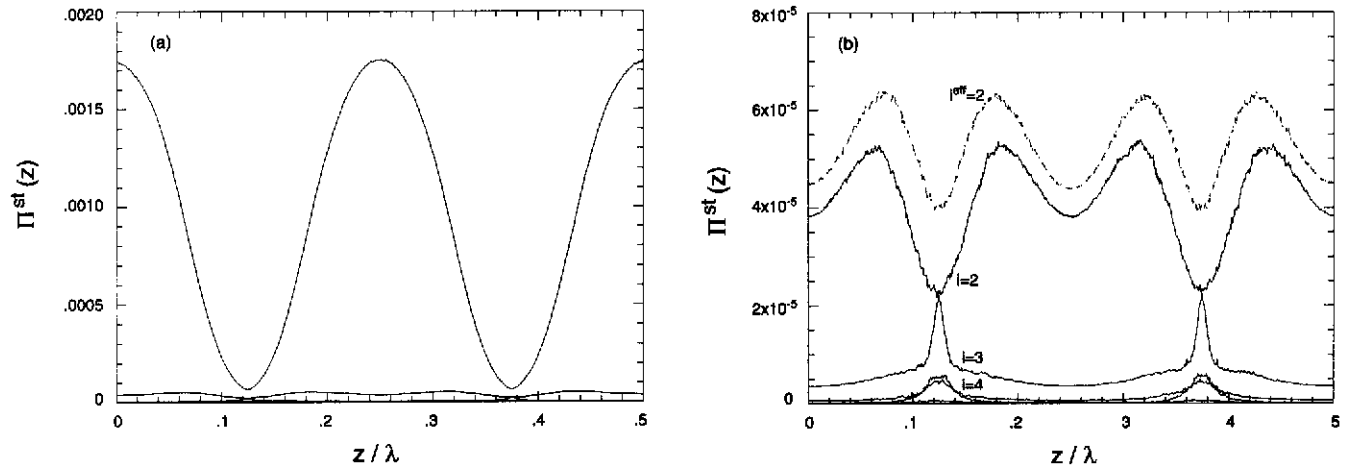

Fig. 6. Steady-state atomic spatial distribution in the lattice for the $J_g = 4 \rightarrow J_e = 5$ transition. (a) Spatial distribution in each potential curve. (b) Spatial distribution for the potential curves u_i with $i \neq 1$. In Figure (b), the dashed line corresponds to the spatial distribution obtained for the effective bi-potential curve u_2^{eff}. As can be clearly seen in Figure (a), the occupation rate of the adiabatic curve u_1 is largely predominant. The calculation has been performed for $\hbar\Delta' = -2000E_R$, $\Delta = -10\Gamma$, with a sample of 10000 atoms, an averaging time of $1000/\Gamma'$, after an evolution of $3000/\Gamma'$ in order to reach the steady state.

potential well regime (domain of linear variation of the temperature curves). In particular, the semiclassical models permit to obtain correct values for the slopes of the temperature variation in this domain and lead to values of the temperature very close to the ones obtained by the quantum model[5]. This agreement is remarkable, if one takes into account the great number of simplifications that have been introduced in the framework of our semiclassical treatment. Hence, it appears that, despite the apparent complexity of optical lattices corresponding to high values of J_g, the underlying basic physics of such lattices is actually quite simple.

The integration time which is necessary for reaching the steady state depends on the potential well depth. In order to overcome this problem, we have chosen a relatively long integration time corresponding to $3000/\Gamma'$. With a time step $dt = 0.02/\Gamma'$, this evolution time corresponds to 150000 statistical realizations. Moreover, each point of the curves of Figure 5 is calculated with an averaging time $t_{av} = 1000/\Gamma'$. Typically, each point calculated using the effective bi-potential model requires a couple of CPU hours on a RISC 6000 3AT computer workstation. This reasonable computing time is another favourable argument for the use of our semiclassical models. Generally, for values of the potential well depth which are well above the threshold of the cooling mechanism, a typical evolution time of $1000/\Gamma'$ is sufficient for the system to reach the steady state. For the sake of definiteness we consider as a limiting value of this regime the value $\hbar\Delta'_{\text{lim}} = 1000E_R$. By contrast, below this limiting value of the potential well depth, the simulations converge much slower towards the steady-state result. Moreover, the results obtained in this shallow potential wells regime correspond to a sharp increase of the atomic temperature and are not in good quantitative agreement with the quantum model. As a matter of fact, for weak values of the potential well depth, our semiclassical approximations may be questionable. In particular, the probability of undergoing a non-adiabatic transition between the different potential curves is stronger for fast atoms, and there is an important fraction of free (and therefore relatively fast) atoms for shallow potential wells. This may explain the high temperatures that we obtain in this regime which are not in good quantitative agreement with the band model[6].

7.1.2 Atomic spatial distribution in the lattice

We now turn to the study of other characteristic stationary properties of the lattice. In Figure 6(a) we have plotted the spatial density as a function of the potential curve, for the $J_g = 4 \rightarrow J_e = 5$ transition and for a maximum light shift corresponding to $\hbar\Delta' = -2000E_R$. It may be seen that the distribution $\Pi^{st}(z)$ has the same $\lambda/4$ spatial periodicity as the potential, the contribution of the potential curve $u_1(z)$ being by far predominant when compared to the ones of the other adiabatic levels. This effect clearly indicates that in steady state the atoms mostly populate the lowest potential curve, as has been previously underlined. The curves presented here are in very good agreement with the ones obtained by using a quantum Monte Carlo wave function simulation [52]. As expected from the study of the previous paragraph, this agreement only holds in the range of deep potential wells where the adiabatic approximation is valid.

[5] We note that the maximum discrepancy between the quantum and the semiclassical results on $p_{\text{r.m.s.}}$ remains generaly lower than 1 $\hbar k$.

[6] Non-adiabatic transitions between potential levels may lead *a priori* to a more efficient Sisyphus cooling. As a result, neglecting such non-adiabatic effects means neglecting an additional cooling mechanism, which explains why we get higher temperatures.

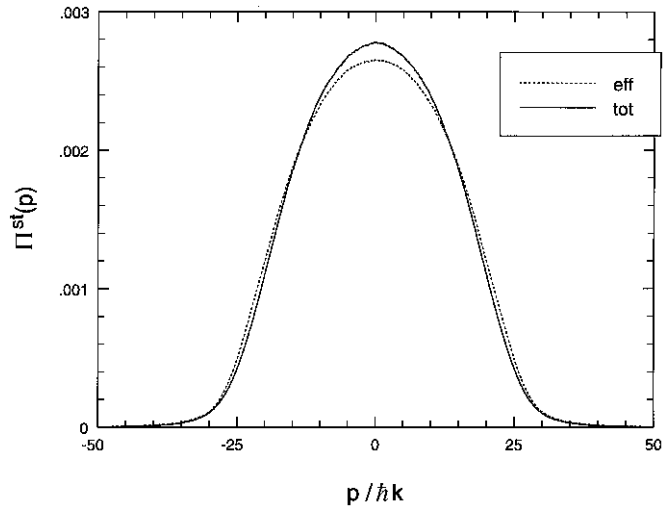

Fig. 7. Stationary momentum distribution in the lattice for the $J_g = 4 \rightarrow J_e = 5$ transition. The full line represents the result of the numerical simulation taking into account the complete internal adiabatic structure. The dotted line corresponds to the simulation using the effective bi-potential method. Both calculations have been performed for an optical potential well depth given by $\hbar|\Delta'| = 2000E_R$, a laser detuning of $\Delta = -10\Gamma$, with a sample of 20000 atoms. The averaging time is $1000/\Gamma'$, after an evolution (in order to reach the steady state) of $3000/\Gamma'$.

Furthermore, we have plotted in Figure 6(b) a zoom of Figure 6(a), showing the spatial distribution on the adiabatic potential curves u_M, for $M \neq 1$, as well as the atomic density associated with the effective level u_2^{eff} (dashed curve). As expected, the density found for the effective level is very close to the one found for the adiabatic level u_2.

7.1.3 Momentum distribution profile

In order to obtain the momentum distribution profile in steady state, we proceed by realizing a histogram of the atomic momenta on a relatively large statistical ensemble. Figure 7 shows the result of such a calculation performed for the $J_g = 4 \rightarrow J_e = 5$ transition, for a potential well depth corresponding to $\hbar\Delta' = -2000E_R$, averaging on 20000 atoms, after a free evolution of $3000/\Gamma'$ for reaching the steady state. We have plotted in the same figure the results obtained using the two different calculation models (*i.e.* the model taking into account all the adiabatic potential levels, or the one making use of the effective bi-potential). The agreement between the two methods is very good. Moreover, we have compared these results to those of a quantum Monte Carlo wave function simulation [52] and observed a very good agreement. Here again, the agreement with quantum calculations is worse for shallower potential wells.

7.2 Discussion of a few physical processes in optical lattices

We have shown so far that our semiclassical models give correct estimates for the atomic temperature of optical lattices corresponding to the deep potential well regime. We wish now to illustrate another particularly interesting aspect of such models, which is the possibility of getting intuitive physical pictures for *a priori* complex fundamental physical mechanisms involved in the dynamics of atoms in optical lattices.

7.2.1 The local cooling mechanism

We shall first concentrate on the study of the nature of the cooling mechanism in 1D optical lattices. The general context of a semiclassical treatment is particularly well adapted to the study of the atom dynamics in terms of single-atom trajectories.

In order to illustrate the differences that exist between the case of the $\frac{1}{2} \rightarrow \frac{3}{2}$ transition and $J \rightarrow J+1$ transitions with $J > 1$, we have represented in Figure 8 typical trajectories for $J = 1/2$ and $J = 4$. The various parts of each trajectory corresponding to different potential curves have been represented using different types of dots, and this permits in particular to give an estimate of the occupation time of each internal level. We have also plotted the time evolution of the mechanical energy of the atom on the same time scale for both cases (Figs. 8(b) and (d)), in order to illustrate better the different energy exchange mechanisms between the atom and the light field.

In the case of the $\frac{1}{2} \rightarrow \frac{3}{2}$ transition, the figure permits to observe the following two features of the atomic motion: on the one hand, the atom spends comparable time intervals on each of the two levels $m = \pm\frac{1}{2}$ of the optical bi-potential, undergoing almost regularly time-spaced jumps between these two levels; on the other hand, the squared variance of the atomic position $\Delta z^2 = \langle z^2 \rangle - \langle z \rangle^2$ shows a rapid increase[7]. An examination of the time evolution of the atomic energy (Fig. 8(b)), permits to see that the cooling mechanism essentially occurs on a spatial scale of *several* potential wells and requires several optical pumping cycles. (It may be noticed that the abrupt changes in the atomic energy are precisely associated with a change of the internal sublevel due to optical pumping.)

For the $J_g = 4 \rightarrow J_e = 5$ transition, the typical atomic trajectory is quite different, as seen in Figure 8(c). One first notices that during the longest part of the trajectory the atom remains in the lowest potential curve (curve u_1), undergoing a few optical pumping cycles towards the other potential curves. Furthermore, in most cases, the atomic motion is principally restricted to the lowest two potential curves u_1 and u_2. The low departure rate from the lowest potential curve towards the other curves in the vicinity of

[7] For potential well depths much more shallower than the one corresponding to Figure 8(a), it is possible to observe trajectories for which the atom covers very long distances without being trapped in a potential well [53].

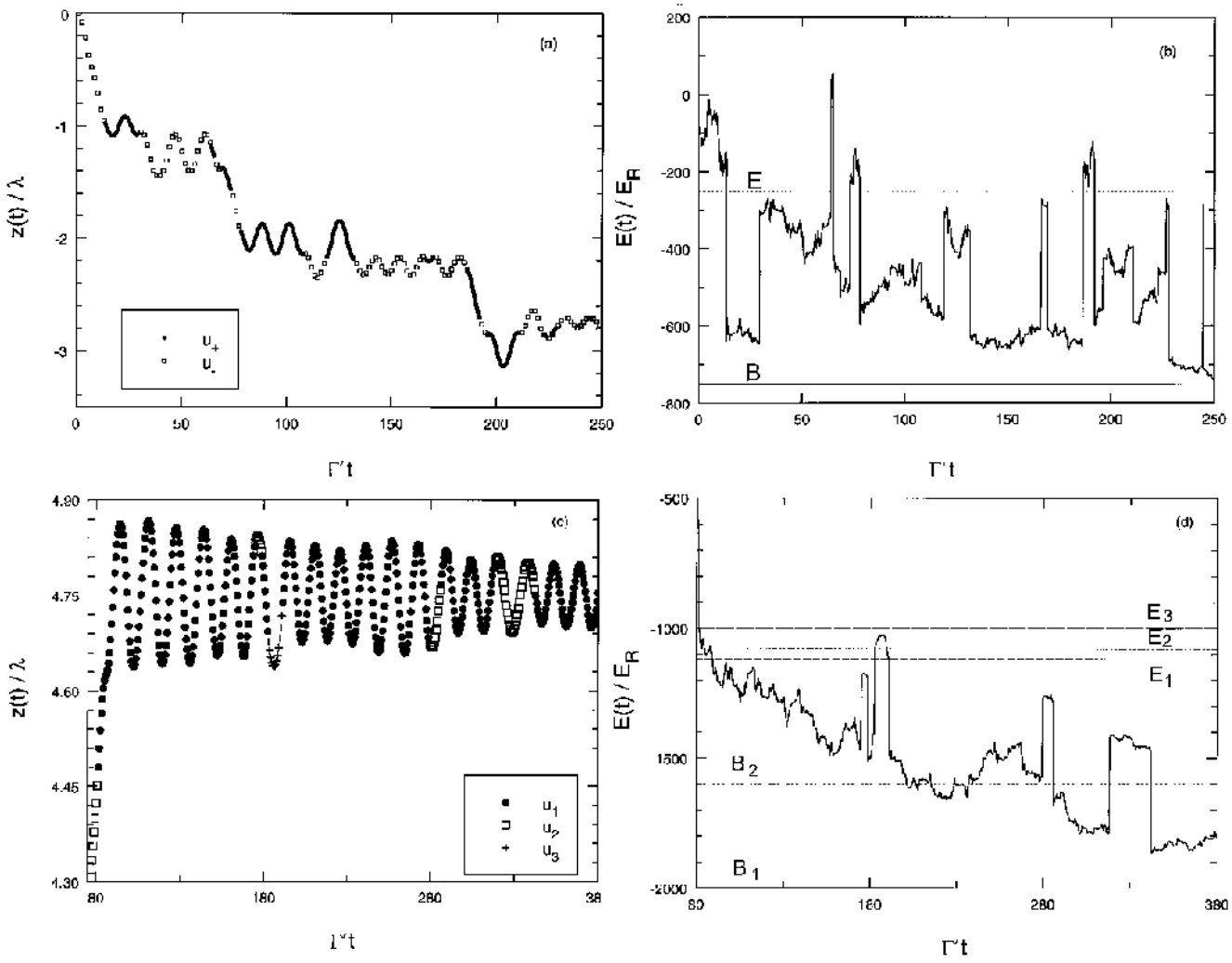

Fig. 8. Illustration of typical "trajectories" followed by an atom in a 1D lattice and atomic energy diagrams as a function of time (in $1/\Gamma'$ units). (a) Trajectory and (b) variation of the total energy of the atom in the case of the $J_{\rm g} = \frac{1}{2} \rightarrow J_{\rm e} = \frac{3}{2}$ transition: the spatial scale of cooling corresponds to several potential wells. The different type of dots indicate the Zeeman sublevel in which the atom evolves. The horizontal lines of Figure (b) labelled B and E represent, respectively, the energy levels of the bottom and of the edge of the optical bi-potential wells. The calculation has been performed for $U_0 = 500 E_{\rm R}$ and $\Delta = -10\Gamma$. (c) Trajectory and (d) total energy of the atom as a function of time, for the case of the $J_{\rm g} = 4 \rightarrow J_{\rm e} = 5$ transition. The spatial scale of cooling is a fraction of an optical wavelength. The various parts of the trajectory associated with different adiabatic potential curves have been represented using different types of dots. The horizontal lines of Figure (d) labelled B_i and E_i represent, respectively, the energy levels of the bottom and the edge of the optical potential well u_i. The parameters of the numerical simulation are $\hbar\,|\Delta'| = 2000 E_{\rm R}$ and $\Delta = -10\Gamma$.

the bottom of the potential wells is due to the very weak value ($\sqrt{1/45}$) of the Clebsch-Gordan coefficient that couples $|\mathrm{g}, \pm 4\rangle$ to $|\mathrm{e}, \pm 3\rangle$. This is because the minima of the potential curve u_1 are located at sites where the light polarization is purely circular. At these locations, the internal state $|\Phi_1\rangle$, associated with u_1, perfectly overlaps with the Zeeman sublevel $m = +4$ (resp. $m = -4$) for a σ^+ (resp. σ^-) site. Moreover, we remark that the atom remains spatially localized on the spatial extent of a single potential well, during considerably long time intervals.

Within the framework of the adiabatic approximation it is therefore possible to extract an interesting feature of the cooling process, by invoking a local Sisyphus cooling mechanism, taking place within a *single* potential well. In order to illustrate this mechanism, let us consider an atom evolving on the lowest potential curve (curve u_1). This atom climbing up a potential hill has some probability to be optically pumped in the upper potential curve u_2, because the departure rate γ_{12} takes significant values away from the minima of u_1. From this point, the atom may return towards the bottom of the potential well u_2, where an optical pumping process brings it in u_1 (the departure rate towards u_1 is a maximum near the bottom of the potential wells of u_2). During such a cycle, the atom loses energy on average, because it spends more of its kinetic energy climbing a steep potential well than it regains

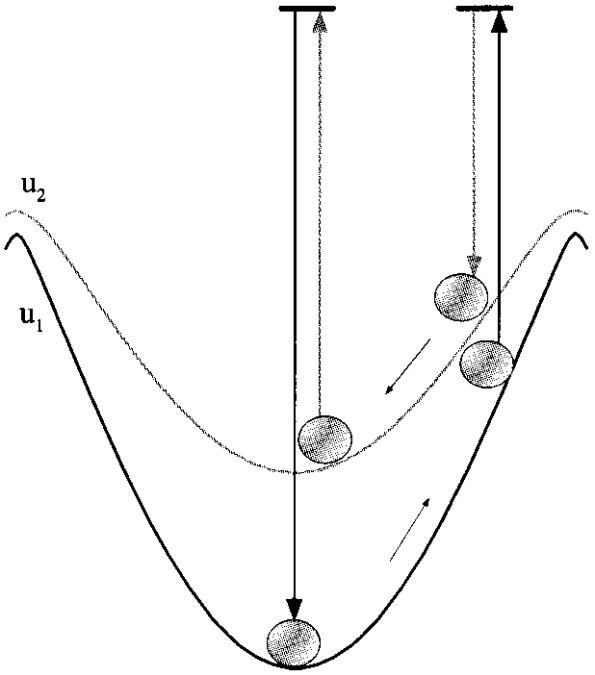

Fig. 9. Local "Sisyphus" cooling mechanism occurring for $J_g = J \to J_e = J + 1$ atomic transitions ($J > 1$).

on the descent of a shallow one (see Fig. 9). As a consequence, the iteration of this type of cycles leads to a local Sisyphus cooling mechanism.

The existence of a local cooling mechanism may explain why the adiabatic approximation (which is well justified near the bottom of the potential wells) leads to very good estimates of the temperature of the lattice. However, it should be noticed that the local cooling mechanism is not self-sufficient for giving a complete description of the cooling occurring in optical lattices. An atom eventually changes potential well and therefore a non-local cooling mechanism is also involved. The question of local *vs.* non-local cooling has been addressed recently by I. H. Deutsch *et al.* [54] in the framework of a different approach, involving an analysis of the system on the basis of the localized Wannier states. This approach led to the conclusion that for shallow potential wells (on the order of a few hundred recoil energies) and for a $J_g = 2 \to J_e = 3$ transition the cooling mechanism is dominated by hopping between different sites rather than by local cooling.

7.2.2 Paramagnetism of optical lattices

As has been recently shown, optical lattices subject to a longitudinal magnetic field exhibit paramagnetism [13–15]. Moreover, in the low magnetic field regime, a spin temperature associated with the internal degrees of freedom was introduced and shown to be on the order of magnitude of the kinetic temperature [14]. So far, all theoretical studies relative to these magnetic properties of optical lattices have been performed using the band model. In this paragraph we show that these properties can also be understood and characterized in the framework of the effective bi-potential semiclassical approach.

As previously, we focus on the case of the $J_g = 4 \to J_e = 5$ atomic transition and of the 1D lin⊥lin configuration, but we now also consider a weak longitudinal magnetic field $\mathbf{B} = B_0 \mathbf{e}_z$. In the presence of the magnetic field the effective Hamiltonian (Eq. (5)) becomes

$$H_{\text{eff}} = \frac{P^2}{2M} + \hbar\Delta' \widehat{A}(z) + \frac{\hbar\Omega_B}{2J_g}\widehat{J}_z, \tag{25}$$

where $\hbar\Omega_B$ stands for the relative Zeeman shift between the outermost magnetic levels $m = 4$ and $m = -4$. We first find the adiabatic eigenstates of the Hamiltonian (25) and consequently deduce the associated effective motion coefficients, as explained in Section 5; second, we numerically simulate the atomic motion within the resulting effective bi-potential in order to obtain the steady-state properties of the system.

Let us first discuss the form of the potentials. Figure 10(a) represents the bi-potential corresponding to a light-shift $\hbar\Delta' = -2000E_R$ and to a Zeeman shift $\hbar\Omega_B = -800E_R$; this figure should be compared to Figure 4(a), that was obtained for zero magnetic field. We notice that for $\Omega_B = 0$, two adjacent potential wells corresponding to opposite circular polarizations are totally equivalent. The major effect of the magnetic field is to break this symmetry and to shift oppositely the adjacent potential wells of the curve u_1, associated locally with the Zeeman sublevels $m = 4$ and $m = -4$. Therefore, potential wells associated with a σ^+ polarization (hence with a positive magnetization) become deeper, and potential wells associated with a σ^- polarization (hence with a negative magnetization) become shallower as the magnetic field is increased.

Furthermore, Figure 10(b) shows the spatial variation of the effective optical pumping rates for non-zero magnetic field. As previously, this figure is to be compared to Figure 4(b) that corresponds to the zero-field case. One notices that the magnetic-field-induced modification of these effective quantities is such that the global departure rate from potential wells associated with a σ^- polarization is significantly increased with respect to the ones that correspond to a σ^+ polarization. One therefore expects a net population transfer from the shallower potential wells towards the deeper ones and hence the appearence of an average non-zero magnetic moment in the lattice.

We now proceed as in Section 5 and calculate the steady-state spatial distribution in the lattice for non-zero magnetic field. It may be seen in Figure 11, that the fraction of atoms occupying the deeper potential wells, associated with a σ^+ polarization, is increased with respect to that of the adjacent, shallower potential wells, which are associated with a σ^- polarization. This result confirms the intuitive idea of population transfer between adjacent potential wells that correspond to opposite circular polarizations. It is moreover possible to estimate the ratio, n_+/n_-, between these occupation rates in steady state, by considering the ratio between the surfaces of two adjacent peaks of the spatial distribution curve. Figure 12

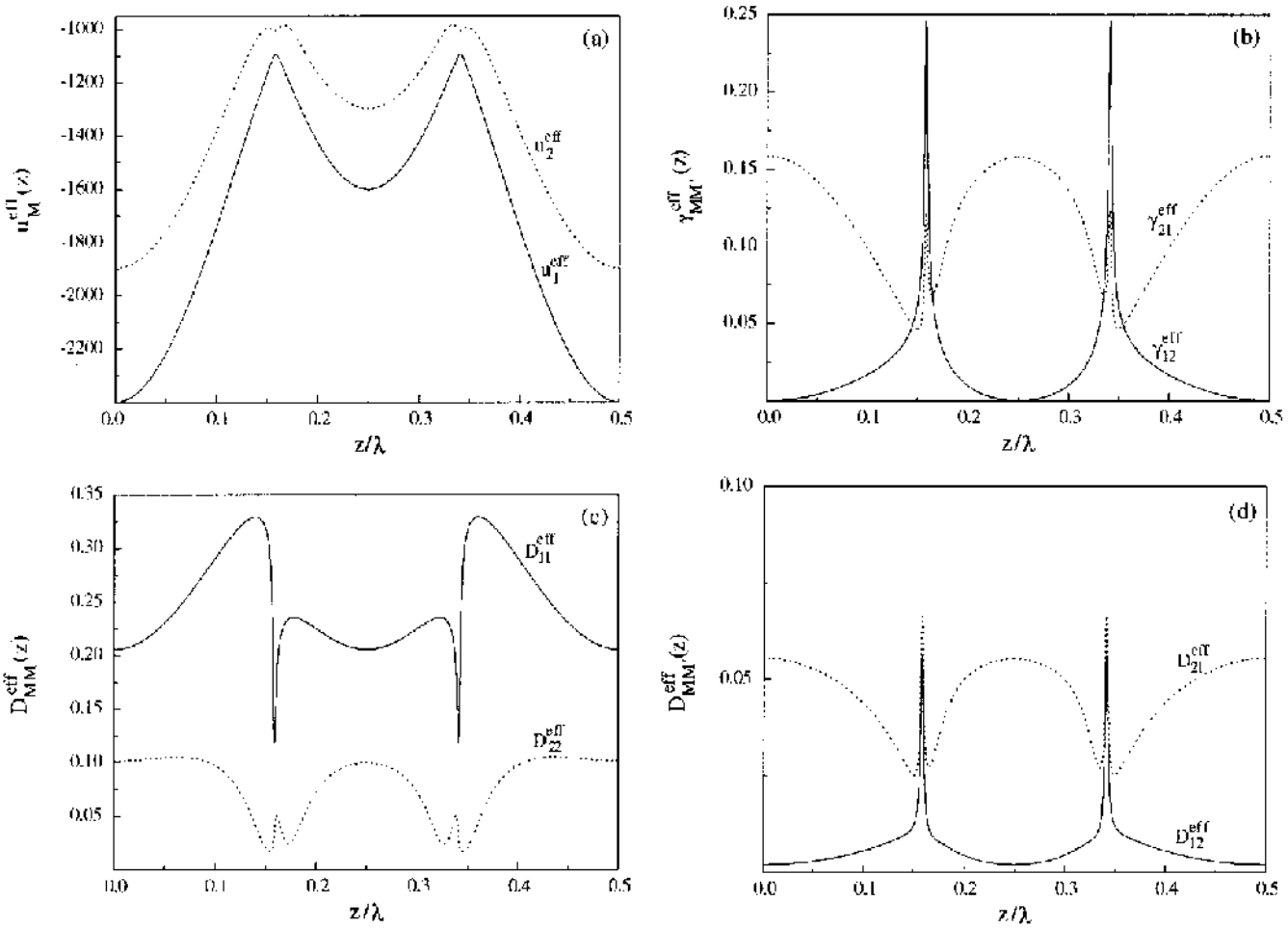

Fig. 10. Effective bipotential and associated coefficients for the $J_g = 4 \rightarrow J_e = 5$ atomic transition in the presence of a weak longitudinal magnetic field. (a) Effective bipotential (recoil units). (b) Effective optical pumping rates (Γ' units). (c) Momentum diffusion coefficients ($\Gamma' \cdot (\hbar \cdot k)^2$ units): diagonal terms. (d) Momentum diffusion coefficients ($\Gamma' \cdot (\hbar \cdot k)^2$ units): non-diagonal term. The figure corresponds to $\hbar\Delta' = -2000E_R$ and $\hbar\Omega_B = -800E_R$.

represents a typical variation curve of the ratio n_+/n_- as a function of the Zeeman shift $\hbar\Omega_B$. This variation has been fitted by an exponential law:

$$\frac{n_+}{n_-}(\Omega_B) = \exp\left(-\frac{\hbar\Omega_B}{k_B T_s}\right). \quad (26)$$

This fit permits to introduce a spin temperature T_s that exhibits a linear variation with the potential well depth $\hbar\Delta'$, for deep potential wells, in agreement with reference [14].

The study of the paramagnetism presented here does not suffer from two problems found in the traditional quantum method (band model and secular approximation): first, because of the resonances found on the variation of the band population with B_0, the different averaged physical observables of the lattice (temperature, magnetization) also acquire sharp resonant variations that look as noise [13,55]. Second, because of the delocalised character of the Bloch eigenfunctions basis, it is not straightforward to calculate the ratio between the occupation rates n_+/n_-.

8 Conclusions

We have presented in this article two semiclassical numerical approaches that permit to perform calculations on 1D optical lattices for realistic atomic transitions $J_g \rightarrow J_e$ involving high values of angular momenta. The first approach consists in numerically simulating the atomic motion within the whole set of adiabatic potential levels that result from the diagonalization of the light-shift operator. The second approach is based on a more dramatic approximation which consists in replacing the exact optical potential by an effective bi-potential. We have shown that the principal features of the atom dynamics are kept by this model. Furthermore, in the deep potential wells regime a very good agreement is obtained with exact quantum models for the kinetic temperature and for the steady-state localization properties of the lattice.

We can conclude from our study that the semiclassical models, based on the adiabatic approximation are quite satisfactory for the description of phenomena which take place inside a single potential well. By contrast, the

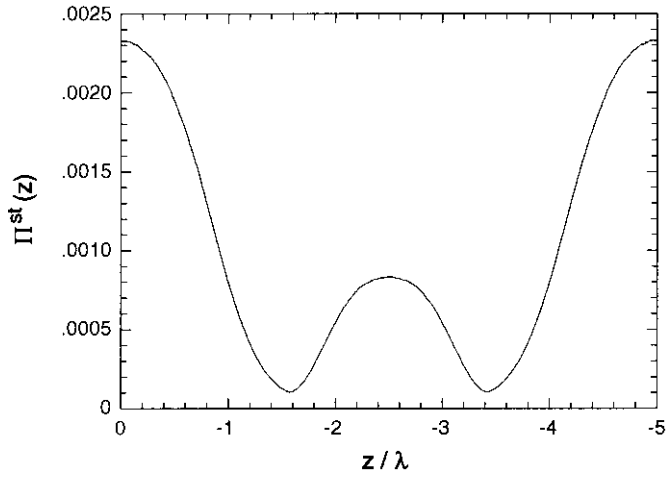

Fig. 11. Steady-state spatial distribution in the lattice for the $J_g = 4 \rightarrow J_e = 5$ transition in the presence of a longitudinal magnetic field. The calculation has been performed for $\hbar\Delta' = -2000E_R$, $\Delta = -10\Gamma$, $\hbar\Omega_B = -800E_R$ with a sample of 5000 atoms. The origin of the z-axis (in optical wavelength units) corresponds to a σ^+ polarized site.

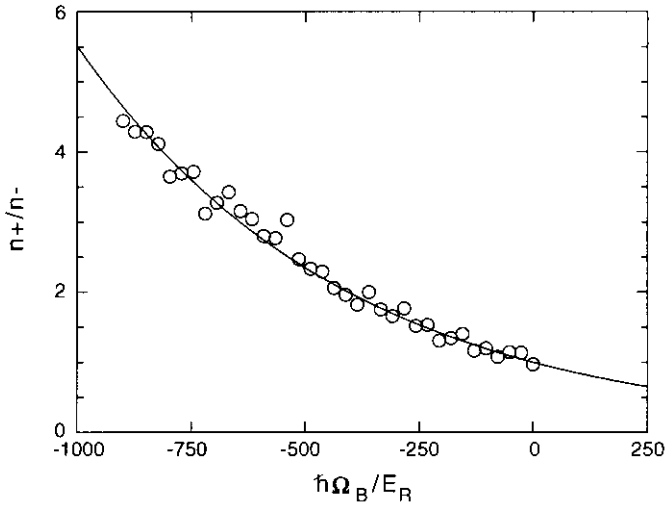

Fig. 12. Ratio n_+/n_- between steady-state occupation rates of potential wells corresponding to opposite circular polarization as a function of the amplitude of the Zeeman shift (open dots). The calculation is performed with a sample of 5000 atoms, for a potential well depth given by $\hbar|\Delta'| = 1500E_R$, and a laser detuning of $\Delta = -10\Gamma$. The variation is fitted by an exponential law (plain curve) that leads to a spin temperature $T_s = 580E_R/k_B$.

validity of such models is not proved for physical phenomena taking place on a spatial extent of several potential wells. In particular, they are questionable for the study of transport phenomena. The remarkable handleability of our models is particularly promising for future extensions in the case of multi-dimensional laser configurations and for complex atomic transitions involved in current experiments.

The comparison with the more traditional quantum models shows the interest of these semiclassical models for the study of bi- and tri-dimensional optical lattices. In the band model the calculation of the atomic wave functions and of the associated stationary populations involve algebraic operations on high-dimension arrays. In a 2D or 3D lattice the physical problem cannot be simply split into several one-dimensional problems, because the optical potential couples the components of the atomic motion along the different directions. In such a case, it is obvious that the dimension of the arrays that one has to diagonalize becomes rapidly excessive. Furthermore, the band model is based on a secular approximation which imposes important restrictions on the validity conditions of the model [32]. Our approaches permit, additionally, to overcome another typical difficulty of the band model which is the existence of population resonances for some values of the potential well depths [33]. These lead to resonant variations of the relevant quantities (temperature, magnetization, etc.) [13,55] which are not observed experimentally. Other quantum models such as the exact quantum wave functions Monte Carlo simulations have already been developed successfully in the case of 3D optical molasses [37]. In particular, the local quantum-jumps method introduced by P. Zoller and coworkers [53] has been successfully used in the characterization of the transport properties of optical lattices. However, such quantum Monte Carlo techniques usually involve very long numerical calculations. Besides these heavy approaches, the semiclassical simulation models appear to be a very promising option, which permits to give at the same time correct quantitative results and clear physical pictures.

Appendix A: Choosing the time step for the integration

A.1 Case of the $J_g = \frac{1}{2} \rightarrow J_e = \frac{3}{2}$ transition

The numerical simulation is realized on a sample of N_{at} atoms, during an averaging time that is given by $T = (N_{step} - N_0)\,dt$; $T_{st} \equiv N_0 dt$ is a sufficiently long time for the system to reach steady state (a typical order of magnitude of T_{st} is given below); N_{step} is the number of statistical realizations. The initial conditions of each realization are chosen randomly. To diminish the statistical uncertainty and to have access to the most probable values of the different observables in the steady state, one has to optimize the choice of the parameters N_{at} and N_{step}. Furthermore, one has to take into account a certain number of restrictions in the choice of the time step dt.

The choice of the integration time step dt should permit to account correctly for the temporal and the spatial variations, in the scale of the atomic motion, of the various relevant physical quantities (radiative forces, optical pumping rates, momentum diffusion coefficients) involved in the equation of motion. On the one hand, the integration time step should be smaller than the typical time scale separating two sequential spin flips due to optical pumping (*i.e.*, $dt \ll \tau_p$, with $\tau_p = 9/(2\Gamma')$) and, on the other hand, the typical distance covered by an atom during the

time interval dt should be much less than $\lambda/2$, which is the typical scale of the spatial variation of the different coefficients characterizing the atomic motion. One can express these two conditions in the following form[8]:

$$\mathrm{d}t \ll \frac{3\Delta/\Gamma}{U_0/\hbar}, \tag{A.1}$$

and:

$$\mathrm{d}t \ll \frac{\lambda/2}{10\hbar k/M}, \tag{A.2}$$

where we have supposed that the typical order of magnitude of the atomic momentum is given by $\overline{p} \simeq 10\hbar k$, for a typical value of the potential well depth characterized by $U_0 \simeq 1000 E_\mathrm{R}$. Generally, the first of these two conditions is much more restrictive than the second one. A typical choice of the time step satisfying both of the above conditions is $\mathrm{d}t = 0.1/\Gamma'$. With such a time step, $N_0 = 4000$ is sufficient in order to reach the steady state.

A.2 Case of higher angular momenta $J_g > 1$

The choice of the time step for the integration of the equations of motion is always limited by the fact that each atom should experience the spatial variations of the different coefficients during its trajectory. A careful look at Figures 3(b) and 4 permits one to see that some of the adiabatic potential curves for the $4 \to 5$ transition, as well as the effective optical pumping rates and momentum diffusion coefficients, exhibit sharp local variations at the scale of $\lambda/1000$. One must therefore choose a time step $\mathrm{d}t$, such that the typical distance covered by an atom during $\mathrm{d}t$ is on the order of $10^{-3}\lambda$:

$$v \cdot \mathrm{d}t \lesssim 10^{-3}\lambda. \tag{A.3}$$

Assuming that the average atomic velocity v is of the order of $10\hbar k/M$ (which is of course only a rough estimate, corresponding to a typical potential well depth of $1000 E_\mathrm{R}$), we are led to the following restrictive condition:

$$\Gamma' \cdot \mathrm{d}t \lesssim 10^{-3}\frac{\hbar\Delta'/E_\mathrm{R}}{\Delta/\Gamma}. \tag{A.4}$$

This condition provides an upper limit for the choice of the integration time step, as a function of the potential well depth and of the laser detuning. One could then naively argue that the use of an infinitely small time step is satisfactory. However, it should be underlined that without making use of the delay function [56], one has to consider a lower boundary for the value of $\mathrm{d}t$, knowing that a very small integration time step would lead to a very small probability for the atom of changing potential level and that the random number generator is not totally uniform for such small values [57][9]. Generally, for a laser detuning of $\Delta = -10\Gamma$, a time step $\mathrm{d}t = 0.02/\Gamma'$ satisfies both of the above restrictive conditions.

The simulation presented in this paper generally corresponds to a sample of $N_\mathrm{at} = 5000$ atoms, and to $\Delta = -10\ \Gamma$[10]. The initial spatial distribution of the atoms is assumed to be uniform, their initial momentum p_in being also uniformly distributed in the interval $[-20\hbar k, 20\hbar k]$ and the initial potential sublevel is obtained randomly. Generally, for values of the potential well depths relatively large compared to the threshold of the Sisyphus cooling mechanism, the steady state is reached after a time evolution of approximatively $1000/\Gamma'$. By contrast, we have observed that numerical simulations performed for relatively small potential well depths ($\hbar\Delta' \lesssim 800 E_\mathrm{R}$) needed much longer integration times for reaching the steady state. As a matter of fact, in this range of parameters, the use of the adiabatic approximation becomes questionable and the results of the semiclassical model may lose their accuracy.

Appendix B: The gauge potential

The adiabatic approximation that we have used in the paper consists more rigorously in neglecting the coherences of the density matrix between states $|\Phi_i\rangle$. One can show that the adiabatic approximation is equivalent to supposing that the Wigner matrix $w(z,p,t)$ is diagonal in the $|\Phi_i\rangle$ basis, but the effective Hamiltonian (5) involved in the equation of motion should be replaced by [50]

$$H_\mathrm{eff} = \frac{(\mathbf{p} - \boldsymbol{\mathcal{A}})^2}{2M} + \widehat{\Lambda}(\mathbf{r}) + \mathcal{V}(\mathbf{r}). \tag{B.1}$$

This new expression of the effective Hamiltonian takes into account two different contributions

– A first term accounting for a *vector* potential $\boldsymbol{\mathcal{A}}$, whose diagonal elements in the $|\Phi_i\rangle$ basis can be written as:

$$\boldsymbol{\mathcal{A}}_i(\mathbf{r}) = \langle\Phi_i|\,\boldsymbol{\mathcal{A}}(\mathbf{r})\,|\Phi_i\rangle = i\hbar\,\langle\Phi_i|\,\boldsymbol{\nabla}\Phi_i\rangle. \tag{B.2}$$

– A second term representing a *scalar* potential, that can be expressed in the following way:

$$\mathcal{V}_i(\mathbf{r}) = \frac{1}{2M}\left[\langle\Phi_i|\,\boldsymbol{\mathcal{A}}^2(\mathbf{r})\,|\Phi_i\rangle - \langle\Phi_i|\,\boldsymbol{\mathcal{A}}(\mathbf{r})\,|\Phi_i\rangle^2\right]. \tag{B.3}$$

In the case where the adiabatic states have real components in the ground state Zeeman sublevel basis (which

[8] Another restrictive condition that should be considered here is that the time step should correctly account for the oscillatory motion of a slow atom (*i.e.*, that $\mathrm{d}t \ll 2\pi/\Omega_\mathrm{v}$, Ω_v being the angular vibration frequency at the bottom of the potential wells). For typical orders of magnitude of the various parameters of the lattice, this condition turns out to be more or less equivalent to (A.2).

[9] It should also be noticed that a very small time step would drastically increase the simulation time required to reach the stationary regime.

[10] We have also performed calculations for $\Delta = -5\Gamma$, for the $4 \to 5$ transition, without observing a noteworthy change of the results presented in the paper.

is the case for the 1D lin⊥lin configuration considered here), this expression can be reduced to

$$\mathcal{V}_i(\mathbf{r}) = -\frac{\hbar}{2M}\langle \Phi_i | \boldsymbol{\nabla}^2 \Phi_i \rangle . \quad \text{(B.4)}$$

These potentials are of *topological* nature, since they depend on the spatial structure of the $|\Phi_i\rangle$ states; they essentially depend on the geometry of the laser beams.

In the case of the lin⊥lin laser field configuration and for $J \to J+1$ atomic transitions that we consider here the light-shifts of all the ground state sublevels are large compared to the recoil energy E_{R}. As a result, the adiabatic potentials lead to contributions which are generally larger by several orders of magnitude compared to those of the potentials of equations (B.2) and (B.3) [50]. It is thus generally reasonable to neglect the effect of these potentials, as well as of the other contributions to the different coefficients involved in the semiclassical equations of motion, which are related to the spatial modulation of the adiabatic states[11].

Appendix C: Optical pumping and momentum diffusion coefficients in the adiabatic states basis

In this appendix we give some general expressions for the different coefficients appearing in the equation of motion (23). The expressions are given in the $\{|\Phi_i\rangle\}$ basis, making use of the operators $\widehat{A}(z)$ and $\widehat{B}_q(z)$ (introduced in Eqs. (6) and (12), respectively):

– To zeroth order in $\hbar k/\overline{p}$, one obtains the effect of the optical pumping between the different internal sublevels for a free particle of constant velocity. This effect is characterized by two rates proportional to $\Gamma' = \Gamma s_{\mathrm{L}}/2$:

i. The effective *departure* rate of level i which can be written:

$$\gamma_i = \Gamma' \langle \Phi_i | \widehat{A} | \Phi_i \rangle - \Gamma' \sum_{q=0,\pm 1} \left| \langle \Phi_i | \widehat{B}_q | \Phi_i \rangle \right|^2 . \quad \text{(C.1)}$$

In this expression, the first term describes the global departure from level i, whereas the second term accounts for processes where the atom returns back to its initial level, after having emitted a fluorescence photon of polarization $\boldsymbol{\epsilon}_q$.

ii. The *feeding* rate of the level i from the level j which is given by

$$\gamma_{ji} = \Gamma' \sum_{q=0,\pm 1} \left| \langle \Phi_j | \widehat{B}_q | \Phi_i \rangle \right|^2 . \quad \text{(C.2)}$$

[11] It should be noticed that the contributions of the scalar potential of equation (B.3) may be non-negligible in the vicinity of the avoided crossings between potential curves. In the deep potential wells regime, it is nevertheless still reasonable to neglect this term, since an atom spends most of the time near the bottom of the potential wells.

– The mean radiative force, appearing to the first order in $\hbar k/\overline{p}$ in equation (23), has only a reactive component corresponding to the effect of the adiabatic potentials. The expression of this force for the level i is given by

$$\boldsymbol{\mathcal{F}}_i(z) = -\frac{\mathrm{d}u_i(z)}{\mathrm{d}z}\,\mathbf{e}_z . \quad \text{(C.3)}$$

– Last, the second order terms in $\hbar k/\overline{p}$ are characterized by two types of momentum diffusion coefficients[12]:

i. The coefficients D_{ii}, accounting for the momentum diffusion related to fluorescence cycles in which there is no change of potential curve:

$$\begin{aligned} D_{ii} = {} & \frac{\hbar^2 \Gamma'}{8} \partial_z^2 \langle \Phi_i | \widehat{A} | \Phi_i \rangle \\ & + \frac{\hbar^2 k^2 \Gamma'}{5} \left(\frac{1}{2} \left| \langle \Phi_i | \widehat{B}_0 | \Phi_i \rangle \right|^2 + \left| \langle \Phi_i | \widehat{B}_1 | \Phi_i \rangle \right|^2 \right. \\ & \left. + \left| \langle \Phi_i | \widehat{B}_{-1} | \Phi_i \rangle \right|^2 \right) \\ & - \frac{\hbar^2 \Gamma'}{8} \sum_{q=0,\pm 1} \left(\langle \Phi_i | \widehat{B}_q^\dagger | \Phi_i \rangle \partial_z^2 \langle \Phi_i | \widehat{B}_q | \Phi_i \rangle \right. \\ & - 2 \left| \partial_z \langle \Phi_i | \widehat{B}_q | \Phi_i \rangle \right|^2 \\ & \left. + \langle \Phi_i | \widehat{B}_q | \Phi_i \rangle \partial_z^2 \langle \Phi_i | \widehat{B}_q^\dagger | \Phi_i \rangle \right) . \end{aligned} \quad \text{(C.4)}$$

ii. The coefficients D_{ji}, associated with a fluorescence cycle where the atom switches from the potential curve j to the curve i:

$$\begin{aligned} D_{ji} = {} & \frac{\hbar^2 k^2 \Gamma'}{5} \left(\frac{1}{2} \left| \langle \Phi_j | \widehat{B}_0 | \Phi_i \rangle \right|^2 + \left| \langle \Phi_j | \widehat{B}_1 | \Phi_i \rangle \right|^2 \right. \\ & \left. + \left| \langle \Phi_j | \widehat{B}_{-1} | \Phi_i \rangle \right|^2 \right) \\ & - \frac{\hbar^2 \Gamma'}{8} \sum_{q=0,\pm 1} \left(\langle \Phi_i | \widehat{B}_q^\dagger | \Phi_j \rangle \partial_z^2 \langle \Phi_j | \widehat{B}_q | \Phi_i \rangle \right. \\ & - 2 \left| \partial_z \langle \Phi_j | \widehat{B}_q^\dagger | \Phi_i \rangle \right|^2 \\ & \left. + \langle \Phi_j | \widehat{B}_q | \Phi_i \rangle \partial_z^2 \langle \Phi_i | \widehat{B}_q^\dagger | \Phi_j \rangle \right) . \end{aligned} \quad \text{(C.5)}$$

[12] In the 1D calculations presented here, the different momentum diffusion coefficients are positive. In higher dimensions these coefficients can be locally negative [30].

References

1. See, for example, the special revue on cooling and trapping of atoms in J. Opt. Soc. Am. B **6**, 7 (1989).
2. See, for example, J.-Y. Courtois, G. Grynberg, Europhys. News **27**, 7 (1996), and references therein.
3. P. Verkerk, B. Lounis, C. Salomon, C. Cohen-Tannoudji, J.-Y. Courtois, G. Grynberg, Phys. Rev. Lett. **68**, 3861 (1992).

4. P.S. Jessen, C. Gerz, P.D. Lett, W.D. Phillips, S.L. Rolston, R. Spreeuw, C.I. Westbrook, Phys. Rev. Lett. **69**, 49 (1992).
5. J.-Y. Courtois, G. Grynberg, Phys. Rev. A **46**, 7060 (1992).
6. A. Kastberg, W.D. Phillips, S.L. Rolston, R.J. Spreeuw, Phys. Rev. Lett. **74**, 1542 (1995).
7. P. Verkerk, B. Lounis, C. Salomon, C. Cohen-Tannoudji, J.-Y. Courtois, G. Grynberg, Phys. Rev. Lett. **68**, 3861 (1992); P.S. Jessen, C. Gerz, P.D. Lett. W.D. Phillips, S.L. Rolston, R.J.C. Spreeuw, C.I. Westbrook, Phys. Rev. Lett. **69**, 49 (1992).
8. A. Hemmerich, T.W. Hänsch, Phys. Rev. Lett. **70**, 410 (1993); G. Grynberg, B. Lounis, P. Verkerk, J.-Y. Courtois, C. Salomon, Phys. Rev. Lett. **70**, 2249 (1993).
9. G. Raithel, G. Birkl, A. Kastberg, S. Rolston, W.D. Phillips, Phys. Rev. Lett. **78**, 630 (1997).
10. G. Raithel, G. Birkl, W.D. Phillips, S. Rolston, Phys. Rev. Lett. **78**, 2928 (1997).
11. A. Hemmerich, M. Weidemüller, T. Esslinger, C. Zimmermann, T.W. Hänsch, Phys. Rev. Lett. **75**, 37 (1995).
12. C. Triché, Ph. D. thesis dissertation, Ecole Polytechnique, Palaiseau, France (1997) (unpublished).
13. C. Triché, D. Boiron, S. Guibal, D.R. Meacher, P. Verkerk, G. Grynberg, Opt. Commun. **126**, 49 (1996); K.I. Petsas, J.-Y. Courtois, G. Grynberg, Phys. Rev. A **53**, 2533 (1996).
14. D.R. Meacher, S. Guibal, C. Mennerat, J.-Y. Courtois, K.I. Petsas, G. Grynberg, Phys. Rev. Lett. **78**, 1958 (1994).
15. C. Mennerat-Robilliard, L. Guidoni, K.I. Petsas, P. Verkerk, J.-Y. Courtois, G. Grynberg, Eur. Phys. J. D **1**, 33 (1998).
16. D.L. Haycock, S.E. Hamann, G. Klose, G. Raithel, P.S. Jessen, Phys. Rev. A **57**, R705 (1998).
17. J.-Y. Courtois, S. Guibal, D.R. Meacher, P. Verkerk, G. Grynberg, Phys. Rev. Lett. **77**, 40 (1996); C. Jurczak, J.-Y. Courtois, B. Desruelle, C.I. Westbrook, A. Aspect, Eur. Phys. J. D **1**, 53 (1998).
18. C. Jurczak, B. Desruelle, K. Sengstock, J.-Y. Courtois, C.I. Westbrook, A. Aspect, Phys. Rev. Lett. **77**, 1727 (1996).
19. N.G. Van Kampen *Stochastic Processes in Physics and Chemistry* (North-Holland, Amsterdam, 1989); H. Risken *The Fokker-Planck Equation* (Springer, Berlin, 1984).
20. S. Chu, L. Hollberg, J.E. Bjorkholm, A. Cable, A. Ashkin, Phys. Rev. Lett. **55**, 48 (1985).
21. S. Stenholm, Rev. Mod. Phys. **58**, 699 (1986).
22. V.G. Minogin, V.S. Lethokov *Laser Light Pressure on Atoms* (Gordon and Breach Science, 1987).
23. J. Dalibard, C. Cohen-Tannoudji, in [1], p. 2023; P. S. Ungar, D. S. Weiss, E. Riis, S. Chu, in [1], p. 2058.
24. D. Nienhuis, P. van der Straten, S.Q. Shang, Phys. Rev. A **44**, 462 (1991).
25. K. Mølmer, Phys. Rev. A **44**, 5820 (1991).
26. J. Javanainen, Phys. Rev. A **44**, 5857 (1991).
27. J. Javanainen, J. Phys. B **27**, L47 (1994).
28. T.W. Hodapp, C. Gerz, C. Furthlehner, C.I. Westbrook, W. D. Phillips, J. Dalibard, Appl. Phys. B **60**, 135 (1995).
29. Y. Castin, Ph. D. thesis dissertation, Université Pierre et Marie Curie, Paris, France (1992) (unpublished).
30. Y. Castin, K. Berg-Sørensen, J. Dalibard, K. Mølmer, Phys. Rev. A **50**, 5092 (1994).
31. Y. Castin, J. Dalibard, Europhys. Lett. **14**, 761 (1991).
32. K. Berg-Sørensen, Y. Castin, K. Mølmer, J. Dalibard, Europhys. Lett. **22**, 663 (1993).
33. J.-Y. Courtois, Ann. Phys. **21**, 1 (1996).
34. J. Dalibard, Y. Castin, K. Mølmer, Phys. Rev. Lett. **68**, 580 (1992).
35. For instance, the problem of spontaneous emission is treated in R. Dum, P. Zoller, H. Ritsch, Phys. Rev. A **45**, 4879 (1992).
36. P. Marte, R. Dum, R. Taïeb, P.D. Lett, P. Zoller, Phys. Rev. Lett. **71**, 1335 (1993); R. Taïeb, P. Marte, R. Dum, P. Zoller, Phys. Rev. A **47**, 4986 (1993)
37. Y. Castin, K. Mølmer, Phys. Rev. Lett. **74**, 3772 (1995).
38. C. Salomon, J. Dalibard, W.D. Phillips, A. Clairon, S. Guellati, Europhys. Lett. **12**, 683-688 (1990); C. Gerz, T. W. Hodapp, P. Jessen, K. M. Jones, W. D. Phillips, C. I. Westbrook, K. Mølmer, Europhys. Lett. **21**, 661 (1993).
39. M. Gatzke, G. Birkl, P. Jessen, A. Kastberg, S.L. Rolston, W.D. Phillips, Phys. Rev. A **55**, R 3987 (1997).
40. In the framework of the quantum wave function Monte Carlo model, for instance, one may use complex "detection" methods in order to get a simple representation of an atomic "trajectory". See M. Holland, S. Marksteiner, P. Marte, P. Zoller, Phys. Rev. Lett. **76**, 20 (1996).
41. Y. Castin, J. Dalibard, C. Cohen-Tannoudji, *Light induced kinetic effects on atoms, ions, molecules*, in *Proceedings of the LIKE workshop*, edited by L. Moi (Pisa, 1991).
42. J.-P. Barrat, C. Cohen-Tannoudji, J. Phys. (Paris) **22**, 329 (1961).
43. C. Cohen-Tannoudji, *Fundamental Systems in Quantum Optics*, Les Houches 1990, Session LIII, in *Proceedings of the Les Houches Summer School of Theoretical Physics* edited by J. Dalibard, J.-M. Raimond and J. Zinn-Justin (Elsevier Science, Amsterdam, 1992), p. 1.
44. J. Javanainen, S. Stenholm, Appl. Phys. **21**, 35 (1980).
45. E.P. Wigner, Phys. Rev. **40**, 749-759 (1932).
46. J. Dalibard, C. Cohen-Tannoudji, J. Phys. B **18**, 1661 (1985).
47. P. Marte, R. Dum, R. Taïeb, P. Zolller, Phys. Rev. A **47**, 1378 (1993).
48. L.D. Landau, Z. Phys. Sowjetunion **1**, 89 (1932); C. Zener, Proc. R. Lond. Ser. A **137**, 696 (1932).
49. R. Gupta, J.J. McClelland, P. Marte, R.J. Celotta, Phys. Rev. Lett. **76**, 4689 (1996).
50. R. Dum, M. Ol'Shanii, Phys. Rev. Lett. **76**, 1788 (1996).
51. J. Dalibard, C. Cohen-Tannoudji, J. Opt. Soc. Am. B **2**, 1707 (1985).
52. S. Marksteiner, unpublished (1995).
53. S. Marksteiner, K. Ellinger, P. Zoller, Phys. Rev A **53**, 3409 (1996).
54. I.H. Deutsch, J. Grondalski, P.M. Alsing, Phys. Rev. A, **56**, R1705 (1997).
55. K. I. Petsas, Ph. D. thesis dissertation, Université Pierre et Marie Curie, Paris, France (1996) (unpublished).
56. C. Cohen-Tannoudji, J. Dalibard, Europhys. Lett. **1**, 441 (1986).
57. W.H. Press, B.P. Flannery, S.A. Teukolsky, W.T. Vetterling *Numerical Recipes. The Art of Scientific Computing* (Cambridge University Press, Cambridge, 1964).